# Detection of extensive equatorial plasma depletions after the 2022 Tongan volcanic eruption from multiple geodetic satellite ranging systems

Shin-Chan Han (1)*, Hyosub Kil (2), Richard Ray (3), Frank Lemoine (3), Colin Waters (4)

(1) School of Engineering, University of Newcastle, Callaghan, NSW, Australia
(2) Applied Physics Laboratory, The Johns Hopkins University, Maryland, USA
(3) Geodesy and Geophysics Laboratory, NASA Goddard Space Flight Center, Maryland, USA
(4) School of Information and Physical Sciences, University of Newcastle, Callaghan, NSW, Australia

*Correspondent: shin-chan.han@newcastle.edu.au

Submitted to
JGR Space Physics
27MAR24
Revised 22OCT24

**Abstract**

We present a number of unique observations of ionospheric anomalies following the Hunga-Tonga Hunga-Ha'apai (HTHH) volcanic eruption on 15 January 2022. All are based on non-dedicated geodetic satellite systems: Global Positioning System tracking of Low Earth Orbit (LEO) CubeSats, intersatellite tracking between two GRACE Follow-On satellites, satellite radar altimeters to the ocean surface, and Doppler radio beacons from ground stations to LEO geodetic satellites. Their observations revealed the development of anomalously large trough-like plasma depletions, along with plasma bubbles, in the equatorial regions of the Pacific and East Asian sectors. Trough-like plasma depletions appeared to be confined within approximately ±20° magnetic latitude, accompanied by density enhancements just outside this latitude range. These plasma depletions and enhancements were aligned with the magnetic equator and occurred across broad longitudes. They were detected in regions where atmospheric waves from the HTHH eruption passed through around the time of the sunset terminator. We interpret these phenomena in terms of the E dynamo electric fields driven by atmospheric waves from the eruption. The uplift of the ionosphere beyond satellite altitudes, followed by subsequent plasma diffusion to higher latitudes along magnetic field lines, results in the formation of trough-like plasma depletions around the magnetic equator and density enhancement at higher latitudes. The detection of plasma bubbles in the Asian sector during the non-bubble season (January) is likely associated with the uplift of the ionosphere at the sunset terminator.

**Plain Language Summary**

Satellite-based ranging measurements use radio signals, which are impacted by electrons in the Earth's atmosphere. A correction for electron density must be applied to the ranging measurement prior to its scientific use. We have found that, after the Tonga volcanic eruption on 15 January 2022, the necessary corrections in the equatorial region were much smaller than usual for four geodetic satellites systems including GPS, GRACE Follow-On, satellite altimeters, and DORIS radio beacons. This implies a reduction in electron content in the Earth's ionosphere in the equatorial region. Our observations demonstrate that the spatial and temporal patterns of the reduction are associated with the atmospheric

pressure waves generated by the eruption. We suggest electric fields driven by atmospheric waves from the eruption as the source of equatorial electron density depletions.

**Key points**

- Geodetic satellites detected plasma depletions and enhancements at low latitudes after the Tongan volcanic eruption on 15 January 2022.
- These phenomena were observed within the region affected by the atmospheric waves propagated from the eruption.
- We suggest that E-region dynamo electric fields are a plausible source of the plasma density modulation at low latitudes.

## 1. Introduction

The Earth's ionosphere is the region of the upper atmosphere (approximately 80 – 1,000 km altitude) where extreme ultraviolet and x-ray solar radiation produces a significant amount of ions and electrons. The major constituent of the ionosphere above ~200 km altitude is the oxygen ion ($O^+$). Below that, molecular constituents like nitro oxygen (NO+) and molecular oxygen ions (O2+) dominate. Therefore, the plasma density above 200 km altitude is primarily determined by production, loss, and transportation of $O^+$. The loss rate of $O^+$ is proportional to the number density of nitrogen and oxygen molecules which varies with altitude. Normally, the peak electron density appears at altitudes around 300 km, the result of a tradeoff between solar radiation energy increasing with altitude and atomic oxygen density decreasing with altitude. The maximum electron density varies generally in the range of $10^5$ - $10^6$ electrons/$cm^3$ depending on various factors including local time, latitude, longitude, season, and solar cycle (Kelley, 2009). At low and mid latitudes, the ionospheric height is modulated by electric fields and plasma motion along magnetic field lines driven by neutral winds. The modulation of the ionospheric height also affects the latitudinal plasma distribution and the development of plasma instabilities (Hanson and Moffett, 1966; Kelley, 2009; Kil and Lee, 2013).

Various forms of atmospheric, ionospheric, and oceanic perturbations have been detected after the Hunga Tonga-Hunga Ha'apai (HTHH) volcanic eruption, which occurred on 15 January 2022 shortly after 4:00 UTC (e.g., Aa et al., 2022; Matoza et al., 2022; Themens et al., 2022; Wright et al., 2022). These studies reported the propagation of atmospheric waves with different speeds, the generation of traveling ionospheric disturbances (TIDs), the modulation of ionospheric height, and the development of unexpected plasma instabilities. Initially large-scale TIDs (LSTIDs) with 2-3 times the surface acoustic speed were generated by acoustic shock waves from the eruption and followed by their slowing at distant locations, and subsequently medium-scale TIDs (MSTIDs) propagating at the speed of sound were observed for many hours (e.g., Themens et al., 2022; Zhang et al., 2022).

Two fascinating ionospheric phenomena caused by the volcanic eruption are MSTIDs that propagate with the speed of atmospheric Lamb waves (300-350 m/s) and severe plasma

depletions at low latitudes, measured by ground-based Global Navigation Satellite System (GNSS) station networks and space-weather dedicated satellite missions (Aa et al., 2022; Amores et al., 2022; Harding et al., 2022; Zhang et al., 2022). MSTIDs in the dayside are produced by the direct interaction between plasma and neutral particles along the path of atmospheric waves. Ionospheric perturbations are intensified by electric fields at night, producing stronger MSTIDs. One of the characteristics of MSTIDs at night is the formation of their mirror (or conjugate) structures at magnetic conjugate locations, and this characteristic was identified after the HTHH volcanic eruption (Hong et al., 2022; Lin et al., 2022). Total electron content (TEC) anomalies as large as 10 TECU (1 TECU = $10^{16}$ electrons/$m^2$) travelling with the Lamb waves were also detected at higher altitudes (>550 km) from the constellation of Global Positioning System (GPS)-tracked CubeSats (Han et al., 2022 & 2023). Recent modeling studies by Vadas et al. (2023a & 2023b) also suggested TIDs could have been generated by secondary atmospheric gravity waves in contrast to the leakage of the surface Lamb wave.

The formation of plasma depletions at low latitudes is closely linked to the uplift of the background ionosphere by electric fields and the generation of plasma bubbles (Kil and Paxton, 2006; Lee et al., 2014; Mannucci et al., 2005). Ground events such as volcanic eruptions may launch atmospheric waves that propagate radially away from the epicenter. These waves generate dynamo electric fields in the ionosphere by which the ionospheric height can be lifted or lowered depending on the wind direction. Multiple studies reported the occurrence of the uplift of the ionosphere during the HTHH event (Gasque et al., 2022; Harding et al., 2022; Hong et al., 2022; Huba et al., 2023; Rajesh et al., 2022). The uplift of the ionosphere in the equatorial region results in the transport of equatorial plasma to higher latitudes by the fountain process (Hanson & Moffett, 1966). This process produces an ionization trough near the magnetic equator and ionization crests outside the equatorial region. The uplift of the ionosphere also promotes the development of equatorial ionospheric phenomena known as “plasma bubbles”. Plasma bubbles, characterized by plasma depletions with respect to the background, are produced by the transport of low-density plasma on the bottomside ionosphere to the topside by the generalized Rayleigh-Taylor instability (Huba et al., 2008; Kelley, 2009; Sultan, 1996; Yokoyama et al., 2014).

These two processes (uplift and plasma instability) are considered to be the major sources of the plasma depletions at low latitudes (Kil and Lee, 2013; Lee et al., 2014).

Geodetic satellite ranging systems are sensitive to electromagnetic media. A medium like the ionosphere causes dispersion of electromagnetic waves by altering direction and speed of propagation. The amount of alteration, often quantified as refractivity, depends on the frequency of electromagnetic waves propagating into the electrically charged ionosphere. For precise geodetic ranging, raw ranging measurements (like beat phase or travel time) must be corrected for refraction by the ionosphere (as well as by the troposphere if relevant). Otherwise, ionospheric refraction may introduce tens of meters of systematic delay in, for example, ranging based on GNSS (Seeber, 2003).

The frequency dependence of refractivity facilitates disentangling ranging and ionospheric interference from measurements, which can be achieved by exploiting multi-frequency waves. This is the fundamental reason for using multi-frequency L-band signals (notably L1 and L2) in GNSS. Similarly, the Gravity Recovery And Climate Experiment Follow-On (GRACE-FO) satellites measure inter-satellite distances with Ka- and K-band waves, and this dual frequency is used to remove ionospheric effects on precise phase measurements in the GRACE-FO microwave interferometer (Tapley et al., 2004; Lee et al., 2011). Satellite radar altimeters, such as those onboard the Sentinel-3 satellites, measure the distance between the satellite antenna phase center and the surface of the Earth, and ionospheric refraction is eliminated by using dual-frequency (e.g., Ku- and C-band) radar (Chelton et al., 2001). For the same reason, Doppler Orbitography and Radiopositioning Integrated by Satellite (DORIS) system uses S- and VHF-band microwave signals (Fleury et al., 1991; Willis et al., 2010; Liu et al. 2023).

This study aims to identify the longitudinal extent of trough-like equatorial plasma depletions caused by the HTHH volcanic eruption. Ground-based and space-weather dedicated satellite observations revealed the development of plasma depletions (Aa et al., 2022; Hong et al., 2022), but these observations have large data gaps over the sea. Given the size of the TEC anomalies reported, other geodetic satellite ranging measurements are likely affected by the HTHH eruption. We first review how each of four geodetic techniques,

including GNSS on Low Earth Orbiters, GRACE-FO satellites, satellite altimeters, and DORIS-equipped satellites, is used to derive an ionospheric correction that is related to the amount of electrons integrated over different paths of the radio frequency (RF) wave propagation. Then, we examine the development of large trough-like plasma depletions over extensive regions using the observations from all geodetic techniques. Finally, we discuss the generation mechanism of depletions in association with the global atmospheric wave (Lamb wave) propagation triggered by the HTHH volcanic eruption.

## 2. Geodetic satellite ranging techniques of measuring TEC

### *2.1 High-low GNSS ranging to low Earth orbit satellites*

A radio wave refracts in the ionosphere if the frequency is higher than the plasma frequency. Ignoring the magnetic field, the refractive index ($n$) of plasma in the ionosphere is essentially dependent on the plasma frequency ($f_p$) and the frequency ($f$) of the radio wave through $n = \sqrt{1 - f_p^2/f^2}$. As the plasma frequency increases with electron density, the amount of refraction increases with the electron density and decreases with the square of radio frequency (e.g., Seeber, 2003; Kelley, 2009). Thus, multi-frequency GNSS radio measurements can be used to derive the electron density integrated along the signal propagation (roughly over 20,000 km, although most electrons are concentrated within 1,000 km of the surface).

By forming a linear combination of L1 and L2 carrier phase counts, $\Phi_{A,1}^i$ and $\Phi_{A,2}^i$, also known as geometry-free combination, the TEC between GNSS satellite $i$ and receiver $A$ is

$$TEC_A^i(t) = \left(\frac{c}{f_{L1}}\Phi_{A,1}^i(t) - \frac{c}{f_{L2}}\Phi_{A,2}^i(t)\right) \Big/ \left(\frac{40.3}{f_{L2}^2} - \frac{40.3}{f_{L1}^2}\right) - B_A^i, \#(1)$$

where $c$ is the speed of light in vacuum, and $f_{L1}$ and $f_{L2}$ are the frequencies of L1 and L2 radio waves, respectively. The approximate constant of 40.3 is derived from values of the electron charge and mass as well as permittivity that appears in the plasma frequency $f_p$

(Hartman and Leitinger, 1984; Teunissen and Kleusberg, 1998). The numerator is the difference of the (biased) ranges measured with L1 and L2 carrier phases which is due to the ionospheric refraction being dependent on radio frequency. This TEC is also called 'slant' TEC along the ray path, and must be differentiated from vertical TEC. Equation (1) implies approximately 16 cm path group delay (or phase advance) per 1 TECU ($10^{16}$ electrons/$m^2$) for L1 frequency. It is also noted that the TEC computed with two phase measurements as in equation (1) contains a bias, $B_A^i$, that is a composite of integer ambiguities, initial fractional phases and differential channel biases (Leick, 1995). In this study, we do not estimate the bias term from dual frequency GNSS data and only focus on relative TEC variations.

*2.2 Low-low intersatellite ranging between two GRACE Follow-On satellites*

The GRACE and GRACE-FO microwave interferometers (MWI) measure relative distance changes between two satellites in tandem by exploiting multiple carrier phases generated by two ultra-stable oscillators (USO) and transmitted simultaneously from two transceivers at both satellites. This is called dual one-way ranging (DOWR) and is designed to eliminate low frequency drift errors of USOs in two satellites without explicit modeling of oscillator (clock) error (Thomas, 1999). In addition, the MWI uses two K- and Ka-band radio frequencies to eliminate the first-order effect of ionospheric phase advance at the satellite altitude (Case et al., 2004; Wen et al., 2017). The second-order effect could be more than three orders of magnitude smaller (e.g., Kedar et al., 2003), which may not be insignificant considering the observation of the first-order effect being as large as several millimeters and the precision of MWI ranging being only several microns (e.g., Landerder et al., 2022). However, the second-order effect depends on the signal propagation direction relative to the local magnetic field and, thus, the DOWR combining carrier phases propagating from both directions can nullify greatly the second-order effect. This is an advantage of DOWR although not widely recognized within the community except in a recent paper by Müller et al. (2022).

Here, we examine how to derive TEC variations between two GRACE-FO satellites from the dual-frequency DOWR MWI by considering only the first order effect (as all higher order

effects are negligible). This TEC represents the path-integrated electron density over ~220 km in distance between the two satellites at ~480 km altitude. The biased intersatellite ranging measurements, $R_K$ and $R_{Ka}$, can be obtained from the DOWR phases, respectively, for the K and Ka-bands, as follows (Wu et al., 2004):

$$R_K(t) = \frac{c}{f_K^A + f_K^B}\left(\Phi_K^{A,B}(t) + \Phi_K^{B,A}(t)\right), \#(2)$$

$$R_{Ka}(t) = \frac{c}{f_{Ka}^A + f_{Ka}^B}\left(\Phi_{Ka}^{A,B}(t) + \Phi_{Ka}^{B,A}(t)\right), \#(3)$$

where $c$ is the speed of light in vacuum, $f_K$ and $f_{Ka}$ are the K- and Ka-band frequencies, respectively, separately operated at USOs of satellites A and B (as indicated by the super-script), and $\Phi_{K\ or\ Ka}^{A,B}$ and $\Phi_{K\ or\ Ka}^{B,A}$ represent the one-way phase from satellite A to B and from B to A, respectively; and these phase measurements are available for both K- and Ka-bands as indicated in the sub-script.

The two (biased) intersatellite ranging measurements, $R_K$ and $R_{Ka}$, are subject to two different ionospheric effects proportional to the amount of electrons cumulative along the ray path (i.e., TEC) between two satellites and to the inverse of frequency squared of the carrier phases. This leads to ionosphere-free combined intersatellite ranging (with unknown phase biases) such as

$$R_{KBR}(t) = C_{Ka}R_{Ka}(t) - C_K R_K(t), \#(4)$$

where $R_{KBR}$ is the biased range and two constants $C_{Ka}$ and $C_K$ are derived from the K- and Ka-band frequencies and result exactly in $C_{Ka} = 16/7$ and $C_K = 9/7$ within high precision (see Case et al., 2004). This $R_{KBR}$ is further corrected for light time and antenna phase center to derive instantaneous (biased) range that is the fundamental data for the Earth's gravitational analysis (e.g., Kim, 2000).

On the other hand, the (biased) ionospheric path delay (or phase advance) at the Ka-band is simply computed from the difference between $R_{KBR}$ and $R_{Ka}$, that is, $R_{KBR} - R_{Ka} =$

$C_K(R_{Ka} - R_K)$, and it is also available as one of the Level-1B data products (i.e., "iono_corr" within KBR1B). From this ionospheric range effect, we compute the time series of TEC between two GRACE-FO satellites as

$$TEC_{GRFO}(t) = C_K\{R_{Ka}(t) - R_K(t)\}/(40.3/f_{Ka}^2). \#(5)$$

Equation (5) implies approximately 0.4 mm path delay per 1 TECU for Ka band frequency. Using the KBR1B data record, we examine short-baseline (~220 km) TEC anomalies at the satellite altitude with regard to the volcanic eruption event. This measurement is local and differentiated from GNSS TEC measurement over long baselines between LEO and GNSS satellites. Similar to the GNSS TEC, it is a biased TEC measurements as the K- and Ka-band phase ambiguities are not known.

*2.3 Nadir satellite altimeter ranging to sea surface*

Our third geodetic technique for recovering TEC is dual-frequency satellite altimetry. This is a much noisier technique compared with the two ranging types discussed above because it entails ranging off the ocean surface. However, it does allow determination of the absolute TEC (not relative) for the whole ionosphere below the satellite. Unlike the previous phase-based ranging techniques that result in ionospheric phase 'advance' and thus measured range shorter than true range, the altimeter is based on radar pulses that are subject to group refractivity and leads to range 'delay' in measurement. Other than the sign of the ionospheric effect on range measurement, ionospheric phase advance and group delay can be determined using dual-frequency measurements. Although there were other dual-frequency altimeters flying during January 2022 (e.g., Jason-3), here we use data from the Sentinel-3 satellites as they are sun-synchronous (10:00 and 22:00 local time) and thus repeated passes tend to be affected by (somewhat) similar diurnal variability, thereby simplifying comparisons before and after the HTHH event.

In January 2022 there were two Sentinel-3 satellites in operation, A and B, flying at an altitude of approximately 815 km. Each satellite has two altimeters: a primary one (Ku band) at 13.6 GHz and a secondary (C band) at 5.41 GHz (this C-band frequency is slightly below

the comparable frequency used on the Jason satellite altimeters). The altimeter range perturbation caused by ionospheric path delay at frequency $f$ is related to the TEC below the satellite according to (Chelton et al., 2001; Eq. 85):

$$\Delta R_{\mathrm{ion}}(f) = \frac{40.3}{f^2}\,\mathrm{TEC}, \#(6)$$

in meters (and TEC in electrons/m$^2$), which evaluates to approximately 0.218 cm per $10^{12}$ electrons/cm$^2$ for the K-band frequency, or ~2.18 mm per TECU.

Let $f_k$ and $f_c$ be the two altimeter frequencies, and let their ratio be denoted

$$\delta = f_c/f_k = 0.3985.$$

The range perturbation $\Delta R_{\mathrm{ion}}$ at $f_k$ can be determined from the difference between the two measured ranges $R(f_k)$ and $R(f_c)$ (Chelton et al., 2001; Eq. 96):

$$\Delta R_{\mathrm{ion}}(f_k) = a_c[R(f_c) - R(f_k)], \#(7)$$

where

$$a_c = \delta^2/(1-\delta^2) = 0.189.$$

A potentially serious complication arises from the fact that the altimeter range is affected by the ocean sea state, a bias error which itself is frequency dependent. This "sea-state bias" is caused primarily by wave troughs being better reflectors than wave peaks, so the mean reflected power is biased toward troughs (e.g., Walsh et al., 1991; Arnold et al., 1995). Sea-state bias corrections are generally determined separately for each altimeter frequency by regressing altimeter-based sea-surface heights against wave height (and often wind speed as well), after an initial ionospheric correction (e.g., Tran et al., 2021). Here we use non-parametric corrections developed by Tran and her colleagues and supplied by the Sentinel-3

303 project. The final TEC determination then uses (7) after the two ranges, $R(f_k)$ and $R(f_c)$,
304 have been corrected for sea-state bias.
305
306 As noted above, the TEC determined on individual satellite passes is fairly noisy. The
307 standard approach when applying ionospheric corrections to altimeter-based ocean
308 elevations is to smooth raw (typically 1-Hz) ionospheric data along-track over distances of
309 100-150 km (Zlotnicki, 1994). Below we also apply along-track smoothing, but we also show
310 the unsmoothed 1-Hz Sentinel-3 TEC profiles so readers can readily observe the inherent
311 noise levels in these data.
312
313 *2.4 DORIS ground beacons*
314
315 The last geodetic ranging technique of interest is Doppler Orbitography and
316 Radiopositioning Integrated by Satellite (DORIS) (e.g., Willis et al., 2010). DORIS utilizes two
317 RF of 401.25 MHz (VHF) and 2.036 GHz (S-band) continuously emitted from a network of
318 nearly 60 global ground stations (Saunier, 2023). Satellites equipped with DORIS receivers
319 record dual-frequency Doppler shifts that can be used to compute line-of-sight (LOS) range-
320 rate and, thus, changes in the TEC between the ground stations and the satellites (e.g.,
321 Fleury et al., 1991; Bernhardt et al., 2006; Dettmering et al., 2014). Such measured
322 ionospheric group delay or phase advance is corrected for station coordinates and precise
323 orbit determination with DORIS tracking data in real-time or ex post facto for the creation of
324 geophysical products (e.g. Jayles et al., 2015; Lemoine et al., 2016). The ionosphere
325 correction is derived from the DORIS/RINEX tracking data provided by the International
326 DORIS Service (IDS) (Willis et al., 2010). We follow the procedures described by Lemoine et
327 al. (2016) to compute the ionosphere correction for Doppler data. Currently, a number of
328 scientific satellites are equipped with DORIS receivers including Jason-3, Sentinel-3A/3B and
329 Sentinel-6A. The DORIS data cover the layers of the ionosphere up to satellite altitudes as
330 high as 1,300 km, but, in the LOS direction only. This is a sampling geometry that is different
331 from the geodetic methods described earlier, and as such leads to complementary
332 information.
333

We used the DORIS/RINEX-derived ionosphere correction given in range-rate every 10 seconds and integrated over time to determine the relative (biased) TEC change in LOS between the ground stations and the satellites. Typically, 15 minutes of data were available from each station around the equatorial region between a satellite's rise and set, covering roughly 60 degrees or less in latitude.

## 3. Observational results

### *3.1 Measurements of plasma depletion by GNSS, GRACE Follow-On, and radar altimeter satellites*

For GNSS TEC variation, we processed GPS L1 and L2 carrier phase measurements every second, as available from multiple patch antennae of the Spire's 3U CubeSats (Nguyen et al., 2020; Han et al., 2023): (1) from the antenna in the zenith direction of the CubeSats, (2) from the antenna pointing in the velocity direction, and (3) from the antenna pointing opposite to the velocity direction. The first antenna receives signals from GPS satellites above the local horizon of the CubeSats (and they are used typically to determine precise positions of the CubeSats). The last two are designed to measure the signals from GPS satellites at and below the local horizon of the CubeSats, with the local elevation range from 0° down to -21°. The lower bound of the elevation is dependent on the LEO satellite altitude. These GPS data from two side-looking antennae were used to examine line-of-sight (slant) TEC variations between the occulting CubeSats and GPS satellites covering altitudes from the bottom of the ionosphere (~80 km) to the CubeSat altitude (~550 km), in contrast to the high-altitude TEC variation above the CubeSats measured by the zenith-point antenna. The TEC measurements below the local horizon were also converted to electron density profiles in altitude assuming spherically stratified distribution of electrons over the regions of the impact points (where the maximum refractions occur) using the radio occultation geometry and Abel inversion (Hajj et al., 2002).

Figure 1 shows four different cases of GPS and CubeSats, and electron density profiles on three consecutive days of 14, 15 and 16 of January 2022. For each case, the left panel shows the ground tracks of the CubeSat and GPS satellite and location of the HTHH volcano.

The Lamb wave front at the average time of GPS measurements (UTC shown on top of each panel) is also shown with large curves of different colors representing a few hPa variations of surface pressure (Amores et al., 2022). In each case, there are ~15 minutes of GPS data measured from the occulting CubeSat while it crosses over the rim until it loses tracking from the GPS satellite. Figure 1 also illustrates the average location of the occultation tangent points (marked with stars in colors next to CubeSat ground tracks) where the maximum bending of the GPS radio ray takes place (Hajj et al., 2002). The right panel of each case shows the electron density profiles around the tangent points estimated from GPS slant TEC measurements. Note that the GPS electron density is a relative measurement. In these profiles, the minimum value of GPS estimates was matched to that of the International Reference Ionosphere (IRI) model values (Blitza, 2018).

In the first case (Figure 1a), GPS measurements took place between the occulting CubeSat FM143 and GPS G04 at UTC 11:24 and local time (LT) 01:24 on 15 and 16 of January 2022. The CubeSat sampled the electron density changes over the area northeast of the volcano near the geomagnetic equator right after the eastward Lamb wave passed the region on Day 15. The GPS data from 16 January identified a typical electron density profile with rapid increase of electron density from 200 to 300 km followed by gradual decrease at higher altitudes, showing the peak layer formed around 280 km. However, the GPS measurements on Day 15 do not show any substantial change in altitude over the entire F region and thus no peak formed likely due to electrons depleted from the F region. There is no GPS data on 14 of January from the same CubeSat at the same location.

For the second case (Figure 1b), CubeSat FM117 measured the electron density over the area northwest of the volcano near the geomagnetic equator at UTC noon (11:48) and LT midnight (23:48) on three different days. Once again, the measurements were taken after the Lamb wave swept westward over the region on Day 15. The GPS measurements have peak values of 2 and $4.5 \times 10^5$ electrons/cm$^3$ on Day 14 and 16, respectively, at an altitude of 350 km. However, there was no evident electron density peak formed on Day 15 and there is little electron density variation in altitude from 80 to 550 km relative to variation on other days, again indicating possible depletion of electrons from the entire F region.

The third case of GPS TEC measurements (Figure 1c) occurred above the South China Sea by CubeSat FM115 and GPS G08 at UTC 14:00 (LT 22:00) on three different days. The westward propagating Lamb wave passed through the region before the TEC measurements were taken on Day 15. The electron density increased drastically from 200 km to 270 km by as much as 6-7 $\times$ $10^5$ electrons/cm$^3$ and gradually decreased at higher altitudes on Day 14 and 16. However, the electron densities on Day 15 do not change much across 100 – 550 km only varying by 1 $\times$ $10^5$ electrons/cm$^3$, possibly due to electron depletion by 6-7 times the background density within the entire F region (>200 km) compared to other days.

The last example (Figure 1d) is from CubeSat FM119 occulting over west of Peru close to the geomagnetic equator at a similar UTC 14:12 but at local time of early morning around 08:12 and east of the volcano. The region was just behind the eastward propagating Lamb wave. The GPS electron density estimates show similar patterns of vertical electron distribution but the peak value of 8 $\times$ $10^5$ electrons/cm$^3$ and the peak altitudes of 290 and 370 km on both Day 15 and 16 (note that no CubeSat GPS data are available at this location and this time on Day 14). Unlike the previous cases, no depletion was measured on Day 15, although the observation was made after the Lamb waves swept the region.

For all examined cases, the IRI model (not shown in Figure 1), that relies solely on solar and geomagnetic indices, was inefficacious at capturing any plasma anomaly that originated from the volcanic eruption and its associated atmospheric perturbation. The electron depletion was observed from both west and east sides of the volcano where the atmospheric wave propagated in two opposite directions and from the GPS measurements during the local nighttime on Day 15. The last case of Figure 1 shows no depletion, which is possibly due to the measurements occurring during local morning when plasma begins to build up with increasing sun light. Possible dynamo mechanisms of depleting plasma in the F region are discussed in Section 4.

We now examine the electron distribution at satellite altitude of 480 km across all latitudes, as measured by the GRACE-FO K/Ka-band ranging system. During January 2022, the angle between the GRACE-FO satellite orbital plane and the geocentric vector to the sun (known as ‘beta angle’) was ~45 degrees. This puts the ascending tracks of the GRACE-FO satellites

at a local time of approximately 19:55-20:40 (a half orbital period). This orbital configuration allowed them to sample electron density perturbations while the atmospheric Lamb wave propagated over the Pacific after the volcanic eruption on Day 15. During the local nighttime, electron density perturbations can persist due to the absence of solar photoionization.

We processed the GRACE-FO intersatellite ranging data for TEC on 14, 15 and 16 of January 2022. The GRACE-FO ground tracks shifted eastward roughly by 5 degrees of longitude each day. The measurements over the same local time on three consecutive days is ideal for detecting the anomaly induced by the volcanic eruption. As the Earth rotation rate is ~460 m/s at the equator and the Lamb wave speed is 300-350 m/s, the GRACE-FO satellites were able to measure the electron density over the following regions: (1) east of the Lamb wave before the wave arrives (i.e., unperturbed state), (2) inside the regime of the Lamb wave perturbation, (3) west of the Lamb wave before the wave arrives (i.e., unperturbed state); all at the same local time of 19:55-20:40.

Figure 2 shows six cases of GRACE-FO measurements with the left panel of each case showing the ground tracks of the GRACE-FO ascending orbit on three consecutive days along with the Lamb wave fronts (black dashed curves) and the right panel showing the measurements of TEC changes integrated over ~220 km baseline between two GRACE-FO satellites at different average UTC but at almost the same average LT of 20:12 – 20:24. As the GRACE-FO TEC measurements are biased (due to K/Ka-band carrier phase biases), the minimum value of TEC measurements on each track was set equal to that of the IRI model prediction. Note that any remaining bias in the data (not corrected by the IRI model) does not affect our analysis of reporting relative changes over the repeat passes across the entire latitudes.

In the first case of UTC 06:24 (Figure 2a), the GRACE-FO sampled the region outside and east of the Lamb wave while the Lamb wave propagated outward from the HTHH volcano, thus sampling the unperturbed ionosphere. The GRACE-FO TEC measurements do not exhibit any abnormality on 15 of January relative to the measurements on the other days. There

461 are two orders of magnitude variation of TEC across latitude, showing the maximum of
462 several TECU around the geomagnetic equator.
463
464 The GRACE-FO ground tracks shifted westward in the next orbits while the Lamb wave
465 propagated outward from the HTHH volcano and the GRACE-FO satellites sampled the
466 region of atmospheric perturbation at longitudes of 180°, 160°, and 140° E, at UTC 08:00,
467 09:36, and 11:12, respectively (Figures 2b-d). The measurements on 15 January found 1,000
468 times (or even more) reduction in TEC relative to the TEC on the other days. The TEC value
469 of 0.01 TECU over the length of 220 km between two GRACE-FO satellites corresponds to
470 450 electrons/$cm^3$, which is considered to be lower than the typical plasma density at the
471 bottom of the ionosphere (Kelley, 2009). The interpretation of plasma depletions in the
472 equatorial region is not straightforward because multiple processes may contribute to their
473 formation. Irregular density structures are interpreted as signatures of plasma bubbles;
474 however, density depletions approximately 3,000 km wide across the geomagnetic equator
475 are difficult to explain solely by plasma bubbles. The electron density enhancements at
476 18°N and 18°S in geomagnetic latitudes, along with the plasma depletions in the equatorial
477 region, can be understood as a consequence of the fountain effect (Hanson & Moffett,
478 1966). The deep depletions around the magnetic equator are likely caused by the uplift of
479 the F region beyond satellite altitudes.
480
481 The last example of the GRACE-FO measurements took place outside the Lamb wave
482 propagation (Figures 2e and 2f), but west of the Lamb wave (the opposite to the case of
483 Figure 2a). As the Earth rotation was 50% faster than the Lamb wave propagation, the
484 GRACE-FO satellites overtook the Lamb waves from west and east within a few orbital
485 revolutions. Figures 2e and 2f illustrate the measurements west of the Lamb wave front
486 capturing the ionosphere before the Lamb wave arrived. The GRACE-FO measurements
487 look normal, showing the peak electrons near the geomagnetic equator, for three
488 consecutive days just as the case of Figure 2a. No depletion was observed.
489
490 From the observations in Figure 2, we note plasma density enhancements outside the
491 equatorial region, accompanying severe plasma depletions around the magnetic equator
492 (Figures 2b–2d). These enhancements are pronounced in the Northern Hemisphere and are

493 interpreted as ionization crests. The intensities of the ionization crests in the opposite
494 hemispheres can differ due to variations in neutral composition and winds. The coincidence
495 of equatorial plasma depletions and plasma enhancements outside the magnetic equator is
496 also identified from other satellite observations shown below in Figures 3 and 4. As
497 discussed in Section 4, these observations provide insight into the source of equatorial
498 plasma depletions.
499
500 The vertical TEC integrated from the ocean surface to the altimeter satellite altitudes of
501 ~800 km was measured by the nadir-pointing altimeter ranging systems. The Sentinel-3A
502 satellite orbit is sun-synchronous with its ascending track crossing the equator at 22:00 local
503 time. This allowed sampling of the ionosphere in the Pacific during the local nighttime a few
504 hours after the HTHH volcanic eruption. The GRACE-FO satellites also happened to sample
505 the data at a local time of around 20:00. The vertical TEC measurements on three
506 consecutive days (14, 15 and 16 January 2022) are presented along with the ground tracks
507 in Figure 3; the original 1-sec measurements (blue dots) and the 60-sec moving averaged
508 data (magenta curve) are shown. By the times of the satellite passes over the Pacific, the
509 Lamb wave had propagated outward and reached up to 25°N and 45°N on 15 of January,
510 respectively, in Figures 3a and 3b.
511
512 The latitudinal samples of vertical TEC showed a wide region of low density around the
513 geomagnetic equator between 18°S and 18°N, only on Day 15 (Figure 3a). Two different
514 ionosphere models (JPL's Global Ionosphere Maps, GIM; Martire et al., 2024, and NOAA
515 Ionospheric Climatology, NIC09; Scharroo and Smith, 2010) predicted approximately 10
516 TECU around the equatorial region. The measurements from 14 and 16 January are much
517 more consistent with the models than the measurements from 15 January. The second
518 example of vertical TEC is from the subsequent orbit about 90 minutes later but at the same
519 local time (Figure 3b). As in the previous case, the reduction of TEC by as much as 10 TECU
520 is observed on 15 January only. It is also observed that TEC increased up to 30 – 40 TECU
521 around 20 degrees north and south of the geomagnetic equator at the same time of the
522 depletion observed around the geomagnetic equator, similar to the localized increase found
523 by the GRACE-FO observations. Two narrow peaks are more noticeable in Figure 3b. This
524 resembles the intensification of the equatorial ionization anomaly by the fountain effect

(Hanson & Moffett, 1966). Note that GIM is a model integrating TEC measurements from a number of global GNSS stations, while NIC09 is a climatological analysis of GIM. Therefore, the HTHH volcanic eruption effect is not expected from the climatological NIC09 model. It is not clear why the GIM results (available through altimeter geophysical data record) do not present the electron depletion and enhancement as much as seen from the altimeter measurements. This is possibly related to the limited spatial resolution and lack of GNSS stations over ocean regions (Martire et al., 2024), which is also apparent in altimeter/GNSS comparisons of the diurnal cycle (Ray, 2020).

We also examined data from Sentinel-3B which was in the same orbital plane, for the five consecutive orbits on Day 15, along with the Lamb wave propagation model (Figure 4). The first two measurements occurred outside the atmospheric perturbation region while the last three sampled the ionosphere after the Lamb wave had passed, but all are at similar local times. There was clear reduction in TEC observed from the last three cases over the geomagnetic equatorial regions, at least 30 degrees wide in latitude, consistent with the spatial extent of the decrease of horizontal TEC measured by GRACE-FO satellites (Figure 2). Ionization crest features accompanying plasma depletions around the magnetic equator are also visible in Figure 4.

### *3.2. Contrasting electron density measurements across the HTHH Lamb wave*

We found a unique CubeSat observation that demonstrates the association of equatorial plasma depletions with atmospheric waves caused by the volcanic eruption. As mentioned earlier, the Spire CubeSats were equipped with two side-looking antennae pointing in the orbital velocity direction (‘front’) and the opposite (‘back’). This configuration can be exploited to measure contrasting electron density distribution across the Lamb waves even from a single CubeSat. Figure 5a shows the ground tracks of CubeSat FM119 when it crossed the Lamb wave from west to east. The Lamb wave propagated westward while the low inclination CubeSat orbited eastward, and they met at longitude of ~100°E.

On Day 15, the first half of FM119 measurements (the ground track marked red in Figure 5a) took place southwest of Sumatra Island in the Indian Ocean where the Lamb wave

perturbation had not yet reached (i.e., outside of the wave boundary). The back-side antenna of FM119 observed GPS signals from G05 at the local time around 19:24. The electron density profile #2 in Figure 5b was derived from this back-side antenna and G05. The peak density is $4.5 \times 10^5$ electrons/cm$^3$ at an altitude of 410 km. No perturbation or depletion was identified in the region. The same CubeSat FM119 started to track and occult with respect to G08 via the front-side antenna measuring electron density changes over the South China Sea where the Lamb wave had just passed. This second half of the ground track is marked blue in Figure 5a, and the electron density profile #1 in Figure 5b is derived from these data along this track. By comparing profiles #1 and #2, we can identify a significant plasma depletion along the second half of the track. This degree of sudden density change cannot be accounted for by the local time difference between the two tracks. A differentiating factor between the two tracks is the Lamb wave boundary. The first half track (red) lies beyond the Lamb wave boundaries, while the second half track (blue) falls within them. This observation indicates that Lamb waves were responsible for the ionospheric plasma depletion.

For comparison, we examined the data from the same pairs of FM119 and GPS satellites on Day 16. The local times and locations of the observations on Day 16 are almost the same as those on Day 15. As we can see in Figure 5a, the FM119 and GPS satellite ground tracks are close to each other on both days. The electron density profiles over the Indian Ocean (#3) and the South China Sea (#4) on Day 16 are shown in Figure 5b with dashed lines. The electron density profiles on Day 16 do not exhibit any anomalous behavior. Thus, the drastic electron depletion in the entire F region is the phenomenon only over the region disturbed by the atmospheric Lamb wave on the day of the HTHH volcanic eruption. This observation is consistent with the findings from the high-altitude TEC measurements by GRACE-FO. The observations of equatorial plasma depletions over a broad range of longitudes by different geodetic satellites can be explained by either the uplift of the F region above satellite altitude (~500-600 km) or the poleward transport of equatorial plasma as a result of the uplift. This is discussed further in Section 4.

### *3.3. Spatiotemporal variations in ionospheric delay from DORIS radio beacons*

589 Turning to our fourth geodetic technique, we examined these time-integrated DORIS data to
590 validate our observations of the electron depletion as detected with the other geodetic
591 satellite measurements. Figure 6 illustrates three ground tracks of Jason-3 on 14, 15 and 16
592 January 2022 at UTC around 9:00 (top panels) and 21:00 (bottom panels), from the
593 descending and ascending tracks, respectively. The color code indicates the "relative"
594 ionospheric delay correction in meter (proportional to TEC), for which time series are shown
595 in the middle panels (n.b. the absolute values have no meaning). The "U-shaped" variation
596 is typical as the ionospheric delay is largely dependent on the elevation of a satellite seen
597 from a ground station (right panels). There are ionospheric delay changes as much as 4 m
598 for normal days in two different time periods in each day. That change was reduced to 50
599 cm around UTC 9:00 on Day 15 (Figure 6a). This is a couple of hours after the atmospheric
600 Lamb wave passed through the region around the station BETB in Betio, Republic of Kiribati.
601 This is a large electron depletion in the ionosphere, a reduction by as much as 10 times the
602 usual. The electrons recovered fully by sunrise 12 hours later, as seen from the bottom
603 panel of the data around UTC 21:00 (Figure 6b). Note that almost the same results were
604 observed from Sentinel-6A (not shown), as (at this time) it shared the same orbit as Jason-3
605 with a time difference of only 30 seconds.
606
607 Since the depletion propagates with the westward Lamb wave during the local nighttime,
608 we examined other DORIS stations further west. Figure 7 shows three cases from two
609 stations in Guam, US (MLAC) and in Manila, Philippines (MANB) with various available
610 satellites including Jason-3 (or Sentinel-6A) and Sentinel-3A. Figure 7a shows the electron
611 depletion around UTC 11:00 on Day 15 only when the Lamb wave front passed the Guam
612 station MLAC but not the Manila station MANB; the ionospheric delay was 1-6 m on the
613 normal days while it got reduced to 20 cm, and became somewhat erratic, on Day 15. The
614 jump in the measurement on Day 14 is due to loss of DORIS tracking (cycle slip) that
615 resulted in a 'reset' of phase count. When the two pieces are joined together, the delay was
616 about 1 m on Day 14. The reason for the smaller delay on Day 14, relative to the one on
617 Day 16, even though both passes feature similar elevation change, is not known.
618
619 The measurements from MANB to Jason-3 and Sentinel-6A (Figure 7b) show there is no
620 depletion in electrons and ionospheric delay at UTC 10:30 on Day 15, which is similar to

normal days. There are approximately 3-3.5 meters of ionospheric delays observed on all three days (two pieces of the Day 14 measurements need to be combined considering the offset introduced by reset of phase count on Day 14). At the time the DORIS observations took place, the Lamb wave had not yet reached the station and thus the DORIS system must have sampled the unperturbed atmosphere. However, just after the Lamb wave passed the Philippines (MANB), the electron depletion was observed from the MANB station and Sentinel-3A around UTC 14:30, by which time the Lamb wave was approaching India (Figure 7c). The DORIS data show that the ionospheric delay correction was reduced to 10-20 cm from typical values of a few meters and that this is the result of electron depletion in the ionosphere. The appearance of such reduction is consistent with the timing of the Lamb wave arrival, once again suggesting that the source of electron depletion is likely dynamo electric fields driven by westward propagating Lamb waves.

## 4. Discussion

In this section, we discuss the sources of trough-like equatorial plasma depletions across broad longitudes. Various processes, including neutral composition changes, impulsive shock waves and ionospheric uplifts, can be considered as sources of trough-like equatorial plasma depletions during the HTHH volcanic eruption. The volcanic eruption can cause changes in neutral composition by vertical atmospheric expansion including an increase in water vapor in the F region (Choi et al., 2023). Just as impulsive shock waves generated by earthquakes can cause ionospheric plasma depletions via upwelling of the atmosphere or leading to outward plasma flow (Astafyeva et al., 2019; Shinagawa et al., 2013; Zettergren et al, 2017), acoustic shock waves generated by the HTHH volcanic eruption could generate equatorial plasma depletions (Aa et al., 2022; Astafyeva et al., 2022; He et al., 2023). These processes may affect the plasma density in the local region around the epicenter, but the formation of plasma depletions along the magnetic equator is difficult to explain by these mechanisms. The intensity of these processes would be ordered by the distance from the epicenter rather than by magnetic latitude. Alignment of these processes along the magnetic equator has not yet been demonstrated by observations. Additionally, the ionization crest features accompanying equatorial plasma depletions are not explained by the effects of atmospheric expansion and shock waves.

653

654 The development of strong plasma depletions around the magnetic equator, accompanied
655 by density enhancements outside the equatorial region, is a typical characteristic of the
656 equatorial fountain process. An enhanced fountain process after the HTHH volcanic
657 eruption is supported by the Ionospheric Connection Explorer (ICON) satellite observations
658 of upward plasma motion in the F region (Aa et al., 2022; Gasque et al., 2022). These
659 observations are consistent with the detection of intense plasma bubbles in the Asian and
660 Pacific sectors in association with the upward ionospheric drift (Aa et al., 2022; Hong et al.,
661 2022). The ICON observations of strong neutral winds in the Pacific sector (Harding et al.,
662 2022) and the numerical simulations of dynamo electric fields driven by gravity waves (Huba
663 et al., 2023) further support the role of dynamo electric fields.
664

665 Hong et al. (2022) suggested the uplift of the ionosphere to the west of HTHH by the effect
666 of winds driven by the volcanic eruption. Figure 8a (and Figure 4 of Hong et al., 2022)
667 illustrates this process. The Hall current ($\boldsymbol{J}_{\mathrm{H}}$), driven by westward winds ($\boldsymbol{U}$), becomes
668 discontinuous at the terminator due to the day-night difference in Hall conductivity ($\boldsymbol{\sigma}_{\mathrm{H}}$).
669 Consequently, negative charges accumulate at the terminator, causing the ionosphere in
670 the sunlit region to be lifted perpendicular to the eastward electric field ($\boldsymbol{E}$) and magnetic
671 field ($\boldsymbol{B}$), i.e., $\boldsymbol{E} \times \boldsymbol{B}$ drift. This process allows plasma depletion in the equatorial region to
672 persist at night as the lifted region moves into darkness. The ionospheric uplift in the east
673 of HTHH can also be explained by a similar process by changing the wind direction. In the
674 east, as illustrated in Figure 8b, positive charges accumulate at the terminator by eastward
675 winds resulting in the uplift of the ionosphere in the dark region. The optimal time for the
676 development of electric fields is when the passage of the winds coincides with the local
677 sunset. A downward $\boldsymbol{E} \times \boldsymbol{B}$ drift can also be considered as the cause of the plasma
678 depletion in the equatorial region; chemical reactions with molecular gases at lower
679 altitudes reduce the plasma density. However, the enhancement in the plasma density
680 outside the equatorial region accompanied with equatorial plasma depletions is not
681 explained by the downward $\boldsymbol{E} \times \boldsymbol{B}$ drift.
682

683 The magnitude of electric fields would depend on the duration and magnitude of the wind
684 surge and the temporal distance from sunset. Our observations and previous studies show

685 the development of equatorial plasma depletions in the longitude range of 100° – 230°E.
686 The development of equatorial plasma depletions in this longitude region is seen to be
687 related to the occurrence time of the HTHH volcanic eruption around LT 16:30. Earth's
688 rotation speed at the equator (~470 m/s at 100 km altitude) is faster than the propagation
689 speed of Lamb waves (300–350 m/s). In the west of HTHH, the arrival time of the Lamb
690 waves at a local region moves to a later LT as the longitude moves westward. Beyond a
691 certain longitude (~100°E), the Lamb waves cannot reach the sunset terminator. Then, the
692 process illustrated in Figure 8a does not occur. The arrival time of the Lamb waves at a local
693 region also moves to a later LT as the longitude moves eastward in the east of HTHH.
694 Therefore, the process illustrated in Figure 8b would be effective in the longitude close to
695 HTHH. In our observations (CubeSat observation at UTC 14:12 in Figure 1d), TEC depletion is
696 absent around 260°E, even though the Lamb waves have already passed the region when
697 the CubeSat observations were made. Since the CubeSat observation was made after
698 sunrise (LT 08:12), plasma depletions would be filled by photoionization. However, we
699 cannot rule out the absence of plasma depletion in the region throughout the night because
700 the region was too far away from the sunset terminator (after midnight) when the Lamb
701 waves passed the region.
702
703 We explained the dynamo electric fields using the Hall currents in the E region, but
704 Pedersen currents and F region dynamo electric fields also contribute to the vertical plasma
705 motion at the sunset terminator. Numerical simulations are required to address the
706 contributions of different processes. Rajesh et al. (2022) explained the enhancement of the
707 upward velocity during the HTHH volcanic eruption in association with the F region dynamo
708 instead of the E region dynamo due to reduced E region conductivity. However, Gasque et
709 al. (2022) attributed the ICON observations of the F-region vertical plasma motion to the E
710 region dynamo because this interpretation is consistent with the propagation speed of
711 observed atmospheric waves. The observation time of the vertical plasma motion by ICON
712 in the Northern Hemisphere was around 17:00 LT (Gasque et al., 2022), before sunset in the
713 E region in the Southern Hemisphere. Therefore, the E region might dominate the E and F
714 region coupling, causing the F region plasma motion. Our illustration in Figure 8 aligns with
715 this interpretation.
716

## 5. Conclusion

We investigated the ionospheric disturbances in the equatorial region caused by the HTHH volcanic eruption on 15 January 2022 by examining the data from four different geodetic ranging systems: between GPS and CubeSat satellites (L1/L2 bands), between two GRACE Follow-On satellites (K/Ka bands), between altimeter satellites and the ocean surface (C/Ku bands) and between the ground beacon stations and DORIS-equipped satellites (S/VHF bands). These dual-frequency satellite systems were used to measure electron density changes integrated along ray paths in line of sight from transmitters to receivers. Five types of TEC measurements were taken (1) at high altitude above CubeSat satellite altitude of ~550 km, (2) at low altitude below ~550 km, (3) at GRACE Follow-On satellite altitude of ~480 km, (4) for the entire vertical column of ionosphere below the altimeter satellite altitude of 800 km, and (5) in line-of-sight between the ground and satellites above top of the ionosphere. While the CubeSats, altimeter and DORIS satellites sample TEC variations over a wide range of altitude, the GRACE Follow-On satellites sample horizontal TEC variation along the orbit at a fixed altitude.

The observations from these systems reveal the development of anomalous plasma depletions in the equatorial region across a broad longitude range after the HTHH volcanic eruption. On the basis of our observations, the conditions for the development of the depletions are (1) inside the boundary of the Lamb waves produced by the volcanic eruption and (2) close to the sunset terminator when the Lamb waves pass the region. These conditions facilitate the generation of dynamo electric fields, and by which the ionosphere can be lifted to high altitudes resulting in plasma depletion in the equatorial region. However, the dynamical coupling of the ionosphere with other waves such as secondary gravity waves (Vadas et al., 2023a & 2023b) cannot be ruled out. The size and magnitude of depletion by the HTHH volcanic eruption were anomalously large; for example, at the satellite altitude of 500 km, the reduction of electrons by more than 1,000 times was recorded from the GRACE Follow-On K/Ka band ranging system over the extensive areas of ~3,000 km around the geomagnetic equator. Such magnitudes of depletions are unusual phenomena, indicating that Earth's hazardous surface events can be a source of severe ionospheric disturbances.

This study demonstrated the use of geodetic (non-space-weather-dedicated) satellite constellations for capturing ionospheric perturbations induced by ground events. These geodetic satellite systems can be cohesively operated and analyzed to support space weather monitoring and prediction and, possibly, activity concerning navigation, communications, and surveillance systems that may be affected by extreme event irregularities in the ionosphere. All four geodetic techniques (GNSS high-low tracking, radio occultation, low-low intersatellite tracking, and Doppler ground beacon) and increasing number of suitable satellites will produce new opportunities to monitor the ionosphere continuously and to study the atmosphere-surface coupled processes including atmospheric and gravity waves caused by earthquakes, tsunamis, extreme weather, and volcanic eruptions.

**Acknowledgement.** This work was supported by NASA's GRACE and GRACE Follow-On science team project, Australian Research Council Discovery Program projects (DP170100224 & DP240102399), and the projects sponsored by Geoscience Australia, FrontierSI, and NSW Space Research Network (RP220204). HK acknowledges support by NSF-AGS2029840 and NASA-NNH19ZDA001N. We are indebted to two anonymous reviewers who made several valuable suggestions for this work.

**Open Research.** The Spire Global's GNSS/GPS tracking datasets (aka RINEX files) are publicly available via NASA's Commercial Smallsat Data Acquisition Program from the NASA program website https://csdap.earthdata.nasa.gov. The GRACE-FO Level-1B data (KBR1B for K-Band ionospheric correction and GNV1B for orbit) used in this study are publicly available through https://podaac.jpl.nasa.gov/cloud-datasets. Interested readers can begin by searching GRACE-FO under Projects and Level-1B under Processing Levels. The dual-frequency satellite altimeter data (including ionosphere correction) are available at http://rads.tudelft.nl with associated software at https://github.com/remkos/rads. The DORIS/RINEX data are available from the data centers of the International DORIS Service (IDS), at the Institut National de l'Information Géographique et Forestière (IGN-France) and the NASA CDDIS (Noll and Soudarin, 2006; Noll, 2010) as described at https://ids-doris.org/ids/data-products/tables-of-data-products.html

781

782

## References


Aa, E., Zhang, S., Erickson, P. J., Vierinen, J., Anthea, J., Goncharenko, L. P., Spicher, A., & Rideout, W. C. (2022). Significant equatorial plasma bubbles and global ionospheric disturbances after the 2022 Tonga volcano eruption. Space Weather, 20, e2022SW003101.

Amores, A., Monserrat, S., Marcos, M., Argüeso, D., Villalonga, J., Jordà, G., & Gomis, D.(2022) Numerical simulation of atmospheric Lamb waves generated by the 2022 Hunga-Tonga volcanic eruption. Geophysical Research Letters, 49, e2022GL098240.

Arnold, D. V., W. K. Melville, R. H. Stewart, J. A. Kong, W. C. Keller, E. Lamarre (1995), Measurements of electromagnetic bias at Ku and C bands, J. Geophys. Res., 100, 969-980.

Astafyeva, E., Rolland, L., Lognonné, P., Khelfi, K., & Yahagi, T. (2013). Parameters of seismic source as deduced from 1 Hz ionospheric GPS data: Case-study of the 2011 Tohoku-oki event. Journal of Geophysical Research: Space Physics, 118, 5942–5950. https://doi.org/10.1002/jgra.50556

Astafyeva, E., Maletckii, B., Mikesell, T. D., Munaibari, E., Ravanelli, M., Coïsson, P., ... & Rolland, L. (2022). The 15 January 2022 Hunga Tonga eruption history as inferred from ionospheric observations. Geophysical Research Letters, 49(10), e2022GL098827.

Bernhardt, P. A., C. L. Siefring, I. J. Galysh, T. F. Rodilosso, D. E. Koch, T. L. MacDonald, M. R. Wilkens, and G. P. Landis (2006), Ionospheric applications of the Scintillation and Tomography Receiver in Space (CITRIS) used with the DORIS radio beacon network, *J. Geod.*, 80, 473–485.

Bilitza, D. (2018), IRI the International Standard for the Ionosphere, Adv. Radio Sci., 16, 1-11, https://doi.org/10.5194/ars-16-1-2018

Case, K.; Gerhard, K.; Wu, S.C. Gravity Recovery and Climate Experiment (GRACE) Level-1B Data Product User Handbook. JPL D-22027. 2010. Available online: https://opendap.jpl.nasa.gov/opendap/allData/grace/docs/Handbook_1B_v1.3.pdf

Chelton, D. B., J. C. Ries, B. J. Haines, L.-L. Fu, P. S. Callahan (2001), Satellite altimetry, in Satellite Altimetry and Earth Sciences: A Handbook of Techniques and Applications (Ed: L.-L. Fu and A. Cazenave), pp. 1-131, Academic Press.

Choi, J. M., Lin, C. C. H., Rajesh, P. K., Lin, J. T., Chou, M., Kwak, Y. S., & Chen, S. P. (2023). Giant ionospheric density hole near the 2022 Hunga-Tonga volcanic eruption: multi-point satellite observations. Earth, Planets and Space, 75(1), 184.

Dettmering D, Limberger M, Schmidt M (2014) Using DORIS measurements for modeling the vertical total electron content of the Earth's ionosphere. J Geod 88:1131–1143. DOI 10.1007/s00190-014-0748-2

Fejer, B. G., de Paula, E. R., Gonzalez, S. A., & Woodman, R. F. (1991). Average vertical and zonal F region plasma drifts over Jicamarca. Journal of Geophysical Research, 96 (A8), 13,901−13, 906. https://doi.org/10.1029/91JA01171

Fleury R, Foucher F, Lassudrie-Duchesne P (1991) Global TEC measurement capabilities of the DORIS system. Adv Space Res 11(10):51–54. doi:10.1016/0273-1177(91)90321-A

Gasque, L. C., Wu, Y. J., Harding, B. J., Immel, T. J., & Triplett, C. C. (2022). Rapid volcanic modification of the E-region dynamo: ICON's first glimpse of the Tonga eruption. Geophysical Research Letters, 49(18), e2022GL100825.

Hajj, G.A., E.R. Kursinski, L.J. Romans, W.I. Bertiger, S.S. Leroy, (2002), A technical description of atmospheric sounding by GPS occultation, Journal of Atmospheric and Solar-Terrestrial Physics, 64, 451-469.

Han, S.-C., McClusky, S., Mikesell, T. D., Tregoning, P., & Sauber, J. (2022). Looking to the sky for better tsunami warnings. *Eos*, *103*, 20–23. https://doi.org/10.1029/2022EO220519

Han, S.-C., McClusky, S., Mikesell, T. D., Rolland, L., Okal, E., & Benson, C. (2023). CubeSat GPS observation of traveling ionospheric disturbances after the 2022 Hunga-Tonga Hunga-Ha'apai volcanic eruption and its potential use for tsunami warning. Earth and Space Science, 10, e2022EA002586. https://doi. org/10.1029/2022EA002586

Hanson, W. B., & Moffett, R. J. (1966). Ionization transport effects in the equatorial F region. *Journal of Geophysical Research*, *71*(23), 5559–5572. https://doi.org/10.1029/JZ071i023p05559

Harding, B. J., Wu, Y. J., Alken, P., Yamazaki, Y., Triplett, C. C., Immel, T. J. et al. (2022). Impacts of the January 2022 Tonga Volcanic Eruption on the Ionospheric Dynamo: ICON-MIGHTI and Swarm Observations of Extreme Neutral Winds and Currents. Geophysical Research Letters, 49(9), https://doi.org/10.1029/2022gl098577

Hartmann, G., Leitinger, R. (1984): *Range errors due to ionospheric and tropospheric effects for signal frequencies above 100 MHz*. Bull. Geod. 58: 109–136.

He, J., Astafyeva, E., Yue, X., Ding, F., & Maletckii, B. (2023). The giant ionospheric depletion on 15 January 2022 around the Hunga Tonga-Hunga Ha'apai volcanic eruption. Journal of Geophysical Research: Space Physics, 128(1), e2022JA030984.

847 Hong, J., Kil, H., Lee, W. K., Kwak, Y.-S., Choi, B.-K., & Paxton, L. J. (2022). Detection of
848 different properties of ionospheric perturbations in the vicinity of the Korean Peninsula
849 after the Hunga-Tonga volcanic eruption on 15 January 2022. Geophysical Research
850 Letters, 49, e2022GL099163. https://doi.org/10.1029/2022GL099163
851 Huba, J. D., G. Joyce, and J. Krall (2008), Three-dimensional equatorial spread F modeling,
852 Geophys. Res. Lett., 35, L10102, doi:10.1029/2008GL033509.
853 Huba, J. D., Becker, E., & Vadas, S. L. (2023). Simulation study of the 15 January 2022 Tonga
854 event: Development of super equatorial plasma bubbles. Geophysical Research Letters,
855 50(1), e2022GL101185.
856 Immel, T. J., E. Sagawa, S. L. England, S. B. Henderson, M. E. Hagan, S. B. Mende, H. U. Frey,
857 C. M. Swenson, and L. J. Paxton (2006), Control of equatorial ionospheric morphology by
858 atmospheric tides, Geophys. Res. Lett., 33, L15108, doi:10.1029/2006GL026161.
859 Jayles C., Chaveau J.P., Auriol A. (2015). DORIS/DIODE Real-Time Orbit Determination on
860 Board Saral/AltiKa, Marine Geodesy, 38, 233–240, doi: 10.1080/01490419.2015.1015695.
861 Kedar, S., G. A. Hajj, B. D. Wilson, and M. B. Heflin, The effect of the second order GPS
862 ionospheric correction on receiver positions, Geophys. Res. Lett., 30(16), 1829,
863 doi:10.1029/2003GL017639, 2003.
864 Kelley, M. C. (2009). The earth's ionosphere : plasma physics and electrodynamics, San
865 Diego, CA: Academic Press.
866 Kil, H., and L. J. Paxton (2006), Ionospheric disturbances during the magnetic storm of 15
867 July 2000: Role of the fountain effect and plasma bubbles for the formation of large
868 equatorial plasma density depletions, J. Geophys. Res., 111, A12311,
869 doi:10.1029/2006JA011742.
870 Kil, H., and W. K. Lee (2013), Are plasma bubbles a prerequisite for the formation of broad
871 plasma depletions in the equatorial F region?, Geophys. Res. Lett., 40, 3491–3495,
872 doi:10.1002/grl.50693.
873 Kil, H., Oh, S.-J., Paxton, L. J., & Fang, T.-W. (2009). High-resolution vertical drift model
874 driven from the ROCSAT-1 data. Journal of Geophysical Research, 114 (A10).
875 https://doi.org/10.1029/2009JA014324
876 Kil, H., Y. S. Kwak, L. J. Paxton, R. R. Meier, and Y. Zhang (2011), O and $N_2$ disturbances in the
877 F region during the 20 November 2003 storm seen from TIMED/GUVI, J. Geophys. Res.,
878 116, A02314, doi:10.1029/2010JA016227.

879 Kim, J. Simulation Study of a Low-Low Satellite-to-Satellite Tracking Mission. Ph.D. Thesis,
880 University of Texas, Austin, TX, USA, 2000.
881 Landerer, F.W.; Flechtner, F.M.; Save, H.; Webb, F.H.; Bandikova, T.; Bertiger, W.I.;
882 Bettadpur, S.V.; Byun, S.H.; Dahle, C.; Dobslaw, H.; et al. Extending the global mass
883 change data record: GRACE Follow-On instrument and science data performance.
884 Geophys. Res. Lett. 2020, 47, e2020GL088306.
885 Lee, CK., Han, SC., Bilitza, D. *et al.* Validation of international reference ionosphere models
886 using in situ measurements from GRACE K-band ranging system and CHAMP planar
887 Langmuir probe. *J Geod* **85**, 921–929 (2011). https://doi.org/10.1007/s00190-011-0442-6
888 Lee, W. K., H. Kil, Y.-S. Kwak, L. J. Paxton, Y. Zhang, I. Galkin, and I. S. Batista (2014),
889 Equatorial broad plasma depletions associated with the enhanced fountain effect, J.
890 Geophys. Res. Space Physics, 119, 402–410, doi:10.1002/2013JA019137.
891 Leick, A. (1995): *GPS satellite surveying*. 2nd. Edition, John Wiley, New York.
892 Lemoine F.G., Chinn D.S., Zelensky N.P., Beall J.W., Le Bail K. (2016). The development of the
893 GSFC DORIS contribution to ITRF2014, Adv. Space Res., 58(12), 2520–2542, doi:
894 10.1016/j.asr.2015.12.043.
895 Lemoine J.M., Capdeville H., Soudarin L. (2016). Precise orbit determination and station
896 position estimation using DORIS RINEX data, Adv. Space Res., 58(12), 2677–2690, doi:
897 10.1016/j.asr.2016.06.024.
898 Lin, J., Rajesh, P. K., Lin, C. C. H., Chou, M., Liu, J., Yue, J., Hsiao, T., Tsai, H., Chao, H., & Kung,
899 M. (2022). Rapid Conjugate Appearance of the Giant Ionospheric Lamb Wave Signatures
900 in the Northern Hemisphere After Hunga-Tonga Volcano Eruptions. Geophysical Research
901 Letters, 49(8), 1–6. https://doi.org/10.1029/2022GL098222
902 Liu A., Wang N., Dettmering D., Schmidt M., Wang L., Yuan H. (2023). “Using DORIS data for
903 validating real-time GNSS ionosphere maps”, Adv. Space Res., 72(1), 115-128,
904 https://doi.org/10.1016/j.asr.2023.01.050.
905 Mannucci, A. J., Tsurutani, B. T., Iijima, B. A., Komjathy, A., Saito, A., Gonzalez, W. D., et al.
906 (2005). Dayside global ionospheric response to the major interplanetary events of
907 October 29–30, 2003 ‘‘Halloween Storms’’. *Geophysical Research Letters*, *32*, L12S02.
908 https://doi.org/10.1029/2004GL021467

Martire, L., Runge, T.F., Meng, X. et al. (2024). The JPL-GIM algorithm and products: multi-GNSS high-rate global mapping of total electron content. J Geod 98, 44. https://doi.org/10.1007/s00190-024-01860-3

Matoza, R. S. et al. (2022). Atmospheric waves and global seismoacoustic observations of the January 2022 Hunga eruption, Tonga, Science, 377, 95-100. DOI:10.1126/science.abo7063

Müller, V.; Hauk, M.; Misfeldt, M.; Müller, L.; Wegener, H.; Yan, Y.; Heinzel, G. Comparing GRACE-FO KBR and LRI Ranging Data with Focus on Carrier Frequency Variations. *Remote Sens.* 2022, *14*, 4335. https://doi.org/10.3390/rs14174335

Nguyen, V. A., Nogués-Correig, O.,Yuasa, T., Masters, D., & Irisov, V.(2020). Initial GNSS phase altimetry measurements from the spire satellite constellation. Geophysical Research Letters, 47, e2020GL088308. https://doi.org/10.1029/2020GL088308

Noll, C.E, Soudarin L. (2006). On-line Resources Supporting the Data, Products, and Information Infrastructure for the International DORIS Service. *J Geodesy,* 80, 419–427, doi: 10.1007/s00190-006-0051-y.

Noll, C.E (2010). The crustal dynamics data information system: A resource to support scientific analysis using space geodesy, Adv. Space Res., 45(12), 1421–1440, doi: 10.1016/j.asr.2010.01.018.

Rajesh, P. K., Lin, C. C. H., Lin, J. T., Lin, C. Y., Liu, J. Y., Matsuo, T., ... & Tsai, H. F. (2022). Extreme poleward expanding super plasma bubbles over Asia-Pacific region triggered by Tonga volcano eruption during the recovery-phase of geomagnetic storm. Geophysical Research Letters, 49(15), e2022GL099798.

Ray, R. D. (2020). Daily harmonics of ionospheric total electron content from satellite altimetry, J. Atmos. Sol. Terr. Phys., 209, 105423, 10.1016/j.jastp.2020.105423

Saunier J. (2023). The DORIS network: Advances achieved in the last fifteen years, Adv. Space Res., 72, 3–22, doi: 10.1016/j.asr.2022.07.016.

Scharroo, R., Smith, W. H. F. (2010), A global positioning system-based climatology for the total electron content in the ionosphere, J. Geophys. Res., 115, A10318, doi: 10.1029/2009JA014719

Scherliess, L., & Fejer, B. G. (1997). Storm time dependence of equatorial disturbance dynamo zonal electric fields. Journal of Geophysical Research, 102(A11), https://doi.org/10.1029/97JA02165

941 Scherliess, L., & Fejer, B. G. (1999) Radar and satellite global equatorial F region vertical drift
942 model. Journal of Geophysical Research, 104(A4), 6829–6842.
943 https://doi.org/10.1029/1999JA900025
944 Seeber, G. (2003): Satellite Geodesy: Foundations, Methods, and Applications. 2nd Edition,
945 W. de Gruyter, Berlin-New York.
946 Shinagawa, H., Tsugawa, T., Matsumura, M., Iyemori, T., Saito, A., Maruyama, T., et al.
947 (2013). Two-dimensional simulation of ionospheric variations in the vicinity of the
948 epicenter of the Tohoku-oki earthquake on 11 March 2011. *Geophysical Research Letters*,
949 *40*, 5009–5013. https://doi.org/10.1002/2013GL057627
950 Sultan, P. J. (1996). Linear theory and modeling of the Rayleigh-Taylor instability leading to
951 the occurrence of equatorial spread F. Journal of Geophysical Research: Space Physics,
952 101(A12), 26875–26891. https://doi.org/10.1029/96JA00682
953 Tapley B.D., Bettadpur S., Watkins M., Reigber C. (2004). The Gravity Recovery and Climate
954 Experiment: mission overview and early results. Geophys Res Lett .31(9), L09607,
955 https://doi.org/10.1029/2004GL019779.
956 Teunissen, P. J. G., Kleusberg, A. (1998): GPS for Geodesy. Second Edition. Springer-Verlag,
957 Berlin-Heidelberg-New York.
958 Themens, D. R., Watson, C., Žagar, N., Vasylkevych, S., Elvidge, S., McCaffrey, A., et al. (2022).
959 Global propagation of ionospheric disturbances associated with the 2022 Tonga volcanic
960 eruption. Geophysical Research Letters, 49, e2022GL098158.
961 https://doi.org/10.1029/2022GL098158
962 Thomas, J. (1999), An analysis of gravity field estimation based on intersatellite dual one-
963 way biased ranging, JPL Publ. 98-15, pp. 3 – 13, Jet Propul. Lab., Pasadena, Calif., May.
964 Tran, N., D. Vandemark, E. D. Zaron, P. Thibaut, G. Dibarboure, N. Picot (2021), Assessing the
965 effects of sea-state related errors on the precision of high-rate Jason-3 altimeter sea level
966 data, Adv. Space Res., 68, 963-977. DOI: 10.1016/j.asr.2019.11.034
967 Vadas, S. L., Becker, E., Figueiredo, C., Bossert, K., Harding, B. J., & Gasque, L. C. (2023a).
968 Primary and secondary gravity waves and large-scale wind changes generated by the
969 Tonga volcanic eruption on 15 January 2022: Modeling and comparison with ICON-
970 MIGHTI winds. Journal of Geophysical Research: Space Physics, 128(2), e2022JA031138.
971 Vadas, S. L., Figueiredo, C., Becker, E., Huba, J. D., Themens, D. R., Hindley, N. P., ... &
972 Bossert, K. (2023b). Traveling ionospheric disturbances induced by the secondary gravity

973 waves from the Tonga eruption on 15 January 2022: Modeling with
974 MESORAC/HIAMCM/SAMI3 and comparison with GPS/TEC and ionosonde data. Journal
975 of Geophysical Research: Space Physics, 128(6), e2023JA031408.
976 Walsh, E. J., et al. (1991), Frequency dependence of electromagnetic bias in radar altimeter
977 sea surface range measurements, J. Geophys. Res., 96, 20571-20583.
978 Wen, H.; Gerhard, K.; William, B.; Meegyeong, P.; Carly, S.; Felix, L. Gravity Recovery and
979 Climate Experiment (GRACE) Follow-On (GRACE-FO) Level-1 Data Product User Handbook;
980 JPL D-56935. 2019. Available online: https://podaac-tools.jpl.
981 nasa.gov/drive/files/allData/gracefo/docs/GRACE-FO_L1_Handbook.pdf.
982 Willis, P., et al. (2010) The International DORIS Service (IDS): Toward maturity, *Adv. Space*
983 *Res., 45(12)*, 1408–1420, doi: 10.1016/j.asr.2009.11.018.
984 Wu, S.-C., G. Kruizinga, W. Bertiger (2004), Algorithm Theoretical Basis Document for GRACE
985 Level-1B Data Processing V1.1, Jet Propulsion Laboratory, California Institute of
986 Technology, GRACE 327-741 (JPL D-27672)
987 Wright, C., Hindley, N., Alexander, M. J., Barlow, M., Hoffmann, L., Mitchell, C. et al. (2022).
988 Surface-to-space atmospheric waves from Hunga Tonga–Hunga Ha'apai eruption, Nature,
989 609, 741-746. https://doi.org/10.1038/s41586-022-05012-5
990 Yokoyama, T., Shinagawa, H., & Jin, H. (2014). Nonlinear growth, bifurcation, and pinching
991 of equatorial plasma bubble simulated by three-dimensional high-resolution bubble
992 model. Journal of Geophysical Research: Space Physics, 119, 10,474–10,482.
993 https://doi.org/10.1002/2014JA02070
994 Zhang, S. R., Vierinen, J., Aa, E., Goncharenko, L. P., Erickson, P. J., Rideout, W., ... & Spicher,
995 A. (2022). 2022 Tonga volcanic eruption induced global propagation of ionospheric
996 disturbances via Lamb waves. Frontiers in Astronomy and Space Sciences, 9, 871275.
997 Zettergren, M. D., Snively, J. B., Komjathy, A., & Verkhoglyadova, O. P. (2017). Nonlinear
998 ionospheric responses to large-amplitude infrasonic-acoustic waves generated by
999 undersea earthquakes. *Journal of Geophysical Research: Space Physics*, *122*, 2272–2291.
1000 https:// doi.org/10.1002/2016JA023159
1001 Zlotnicki, V. (1994). Correlated environmental corrections in TOPEX/POSEIDON, with a note
1002 on ionospheric accuracy. J. Geophys. Res., 99, 24,907-24,914.
1003
1004

**Figure Caption**

**Figure 1**. CubeSat GPS measurements of electron density (Ne) changes. Each panel, (a) through (d), presents ground tracks of CubeSats and GPS satellites and the atmospheric Lamb wave front at different times in UTC on the days before, on and after the HTHH volcanic eruption. It also shows vertical distribution of electron density (Ne) computed from the slant TEC measurements between CubeSats and GPS satellites. The local time (LT) and UTC time represent the average epoch of the TEC measurements. The CubeSat and GPS satellites repeat their ground tracks roughly within a few hundreds of km every day. This repeated orbital sampling allows us to monitor electron content variations over the same region at the same time but on different days. The geomagnetic equator is depicted as a black curve on the map, the location of HTHH volcano is marked with a magenta triangle, the Lamb wave front is shown in black dashed curve, and lastly, the tangent points are shown in stars next to the CubeSat ground tracks. Four pairs of CubeSat and GPS satellites were examined, including FM143 – G04, FM117 – G31, FM115 – G08, and FM119 – G29, to find changes along the geomagnetic equator over a wide range of longitudes. Three cases of local nighttime measurements, (a)-(c), found substantial reduction in electron density after the Lamb wave passage on the day of HTHH volcanic eruption, while the last case (d) shows no change observed at the local morning time, due possibly to regeneration of plasma. Three different colors are used for three different days. The sunset terminator at the equator at the time of the Day 15 measurements is shown in gray dashed line. This same color and symbol is used throughout all figures in this paper. East of this sunset terminator is the night side.

**Figure 2**. GRACE Follow-On measurements of changes in TEC integrated over ~220 km between two satellites at the altitude of ~480 km, from 6 am to 4 pm in UTC (local time of 8-9 pm) on 14, 15, and 16 of January 2022. Each panel shows the ground tracks of GRACE Follow-On satellites and the Lamb wave front (black dashed curves) propagated from the HTHH volcano (magenta triangle) on 15 of January 2022. The direction of the wave propagation is shown with small arrows. The geomagnetic equator is marked by a heavy black curve. The TEC measurements between the two satellites are presented along the geomagnetic latitude of the midpoint of two satellites and shown in a log scale (as the

change is up to 4 orders of magnitude). Three measurements on three days are compared to highlight the drastically reduced TEC only on the eruption day and only over the region after the volcano-induced Lamb wave passage, i.e., panels of (b) through (d). The measurements outside of the Lamb wave boundary show no change in electron density. This series of measurements clearly suggest the depletion associated with the Lamb wave. It is observed that the volcano-induced TEC reduction at the satellite altitude (~480 km) is from 10 to 0.001 TECU and is as wide as 3,000 km along the geomagnetic equator.

**Figure 3**. Sentinel-3A satellite altimeter measurements of vertical TEC changes on 14, 15, and 16 of January 2022. During UTC approximately 9 to 11 am (local time around 10:30pm), the satellite flew over the Pacific Ocean and detected ionospheric changes associated with the volcano-driven Lamb wave (black dashed curve). The map includes the ground tracks as well as the Lamb wave front at the time of altimeter measurements. The vertical TEC measurements (blue dots) on three consecutive days are compared with two model outputs of JPL's Global Ionosphere Maps GIM (red curve) and NOAA's Ionospheric Climatology NIC09 (yellow curve). The smoothed (60-sec moving average) TEC measurements are also shown for better comparison with the models (magenta curve). On the day of eruption, the vertical TEC measurements along the satellite orbit decreased as much as 10 TECU relative to the model predictions and relative to the measurements on the other ('normal') days. The spatial extent of the TEC depletion is around 3,000 km around the geomagnetic latitude, similar to the GRACE-FO measurements of high-altitude TEC variation.

**Figure 4**. Sentinel-3B satellite altimeter measurements (bottom panels) of vertical TEC changes during the five consecutive ascending orbits (top panels) on 15 of January, from UTC hours from 5 am to 12 pm and Local time around 10 pm. These data allow us to examine the TEC measurements with the Lamb wave propagation every orbit (~100 min sampling). The first two cases (first two left columns) present the data outside the Lamb wave boundary (black dashed curve), while the last three show the measurements inside, but all are nearly at the same local time. The large depletion is found only in the region around the geomagnetic equator and only inside of the Lamb wave boundary.

**Figure 5**. CubeSat GPS measurements of electron density changes across the Lamb wave. This example is similar to Figure 1, but it uses the two GPS antennae pointing in the satellite velocity direction and its opposite. The same CubeSat FM119 tracked GPS satellite G05 from the backward antenna while it picked up G08 through the front antenna. The data on two days of 15 and 16 of January were compared (as no data on 14 of January is available). The pair of FM119 – G05 sampled the electron density outside the Lamb wave above the Indian Ocean while the other pair of FM119 – G08 measured inside the Lamb wave above the Southern China Sea. The four vertical electron density profiles on two days and from two different locations (outside and inside of the wave) are compared in the right panel. It is clear that drastic reduction of electron density was observed only from the inside region and only on the eruption day. This highlights excellent samplings of measuring dynamical ionospheric anomalies associated with the propagating atmospheric perturbation by exploiting the multi-faceted GPS antennae from a single CubeSat.

**Figure 6**. (a) The left panel shows the descending ground tracks of Jason-3 on 14, 15, and 16 January 2022 around the ground station BETB (marked in magenta inverted triangle). The color code presents the time-integrated ionospheric delay in range (i.e., biased ionospheric delay in meter) along the ground track each day. The biased delay and the elevation angle of the satellite seen from the ground station are shown as a time-series in the middle and right panels, respectively, for each track for three different days. The delay varies over ~4 m on normal days, however, there was large reduction in the delay around UTC 9:00 on Day 15, after the Lamb wave passage. (b) The same as (a), but from the ascending track data 12 hours later. This shows the ionosphere returned to its normal condition. For (b), the Lamb wave front was around the antipode near the southern tip of Algeria, which is outside of the map.

**Figure 7**. (a) The same as Figure 6, but between the Sentinel-6A and the ground station MLAC in Guam, USA. It demonstrates large reduction in the ionospheric delay associated with the electron depletion after the Lamb wave passage. (b) The case between Jason-3 and MANB (a ground station in Manila, Philippines) between UTC 10:00 – 11:30, prior to the Lamb wave arrival. (c) The case between Sentinel-3A and MANB after the Lamb wave

passed the region (UTC 14:00-15:00). The reduction in the ionospheric delay was found only after the Lamb wave.

**Figure 8**. Schematic illustration of the generation of electric fields (a) west and (b) east of HTHH in association with the volcanic eruption. Winds ($\boldsymbol{U}$) from the volcanic eruption generate westward (a) and eastward (b) Hall currents ($\boldsymbol{J}_{\mathrm{H}}$) in the E region, and negative (a) and positive (b) charges accumulate at the terminator by the day-night difference of the Hall conductivity ($\boldsymbol{\sigma}_{\mathrm{H}}$). The polarization electric fields ($\boldsymbol{E}$) in the E region map into the F region, resulting in the upward $\boldsymbol{E} \times \boldsymbol{B}$ plasma drift in sunlight (a) and darkness (b).

**Figure 1.**

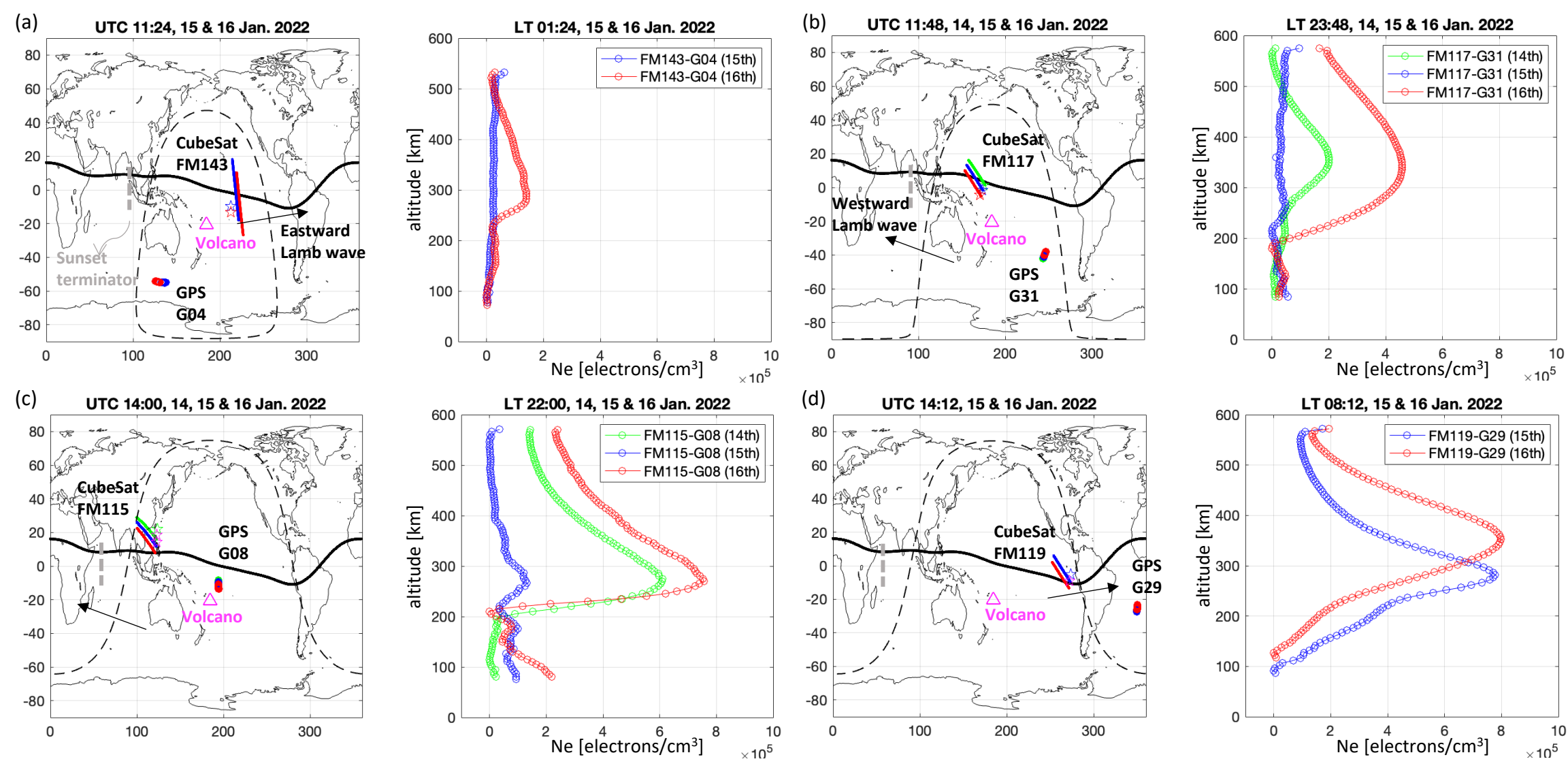
(a)
UTC 11:24, 15 & 16 Jan. 2022
CubeSat
FM143
Volcano
Eastward
Lamb wave
Sunset
terminator
GPS
G04
LT 01:24, 15 & 16 Jan. 2022
FM143-G04 (15th)
FM143-G04 (16th)
altitude [km]
Ne [electrons/cm³]
×10^5
(b)
UTC 11:48, 14, 15 & 16 Jan. 2022
CubeSat
FM117
Westward
Lamb wave
Volcano
GPS
G31
LT 23:48, 14, 15 & 16 Jan. 2022
FM117-G31 (14th)
FM117-G31 (15th)
FM117-G31 (16th)
altitude [km]
Ne [electrons/cm³]
×10^5
(c)
UTC 14:00, 14, 15 & 16 Jan. 2022
CubeSat
FM115
GPS
G08
Volcano
LT 22:00, 14, 15 & 16 Jan. 2022
FM115-G08 (14th)
FM115-G08 (15th)
FM115-G08 (16th)
altitude [km]
Ne [electrons/cm³]
×10^5
(d)
UTC 14:12, 15 & 16 Jan. 2022
CubeSat
FM119
GPS
G29
Volcano
LT 08:12, 15 & 16 Jan. 2022
FM119-G29 (15th)
FM119-G29 (16th)
altitude [km]
Ne [electrons/cm³]
×10^5

**Figure 2.**

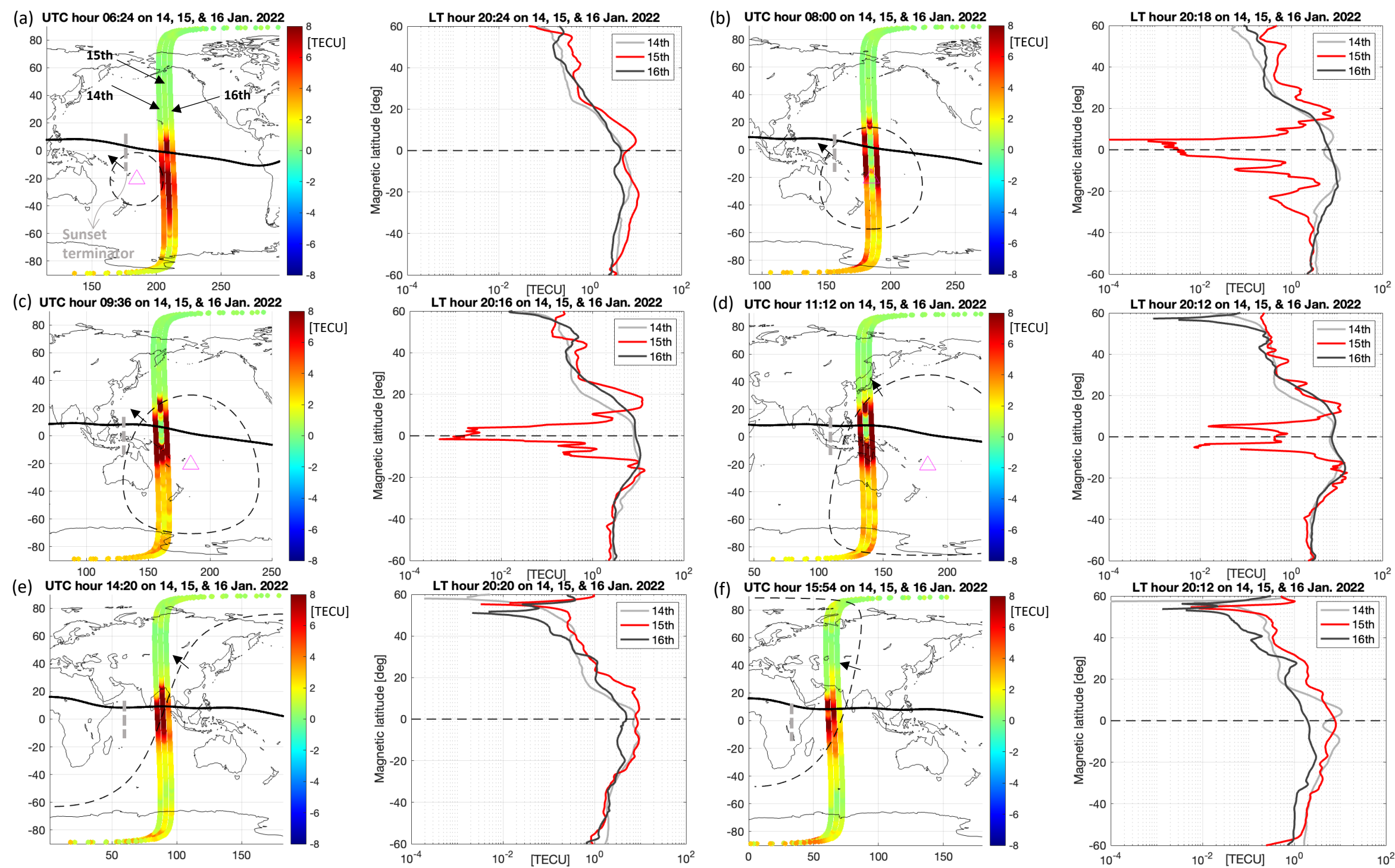
(a) UTC hour 06:24 on 14, 15, & 16 Jan. 2022
15th
14th
16th
Sunset terminator
[TECU]
LT hour 20:24 on 14, 15, & 16 Jan. 2022
14th
15th
16th
Magnetic latitude [deg]
[TECU]
(b) UTC hour 08:00 on 14, 15, & 16 Jan. 2022
[TECU]
LT hour 20:18 on 14, 15, & 16 Jan. 2022
14th
15th
16th
Magnetic latitude [deg]
[TECU]
(c) UTC hour 09:36 on 14, 15, & 16 Jan. 2022
[TECU]
LT hour 20:16 on 14, 15, & 16 Jan. 2022
14th
15th
16th
Magnetic latitude [deg]
[TECU]
(d) UTC hour 11:12 on 14, 15, & 16 Jan. 2022
[TECU]
LT hour 20:12 on 14, 15, & 16 Jan. 2022
14th
15th
16th
Magnetic latitude [deg]
[TECU]
(e) UTC hour 14:20 on 14, 15, & 16 Jan. 2022
[TECU]
LT hour 20:20 on 14, 15, & 16 Jan. 2022
14th
15th
16th
Magnetic latitude [deg]
[TECU]
(f) UTC hour 15:54 on 14, 15, & 16 Jan. 2022
[TECU]
LT hour 20:12 on 14, 15, & 16 Jan. 2022
14th
15th
16th
Magnetic latitude [deg]
[TECU]

**Figure 3.**

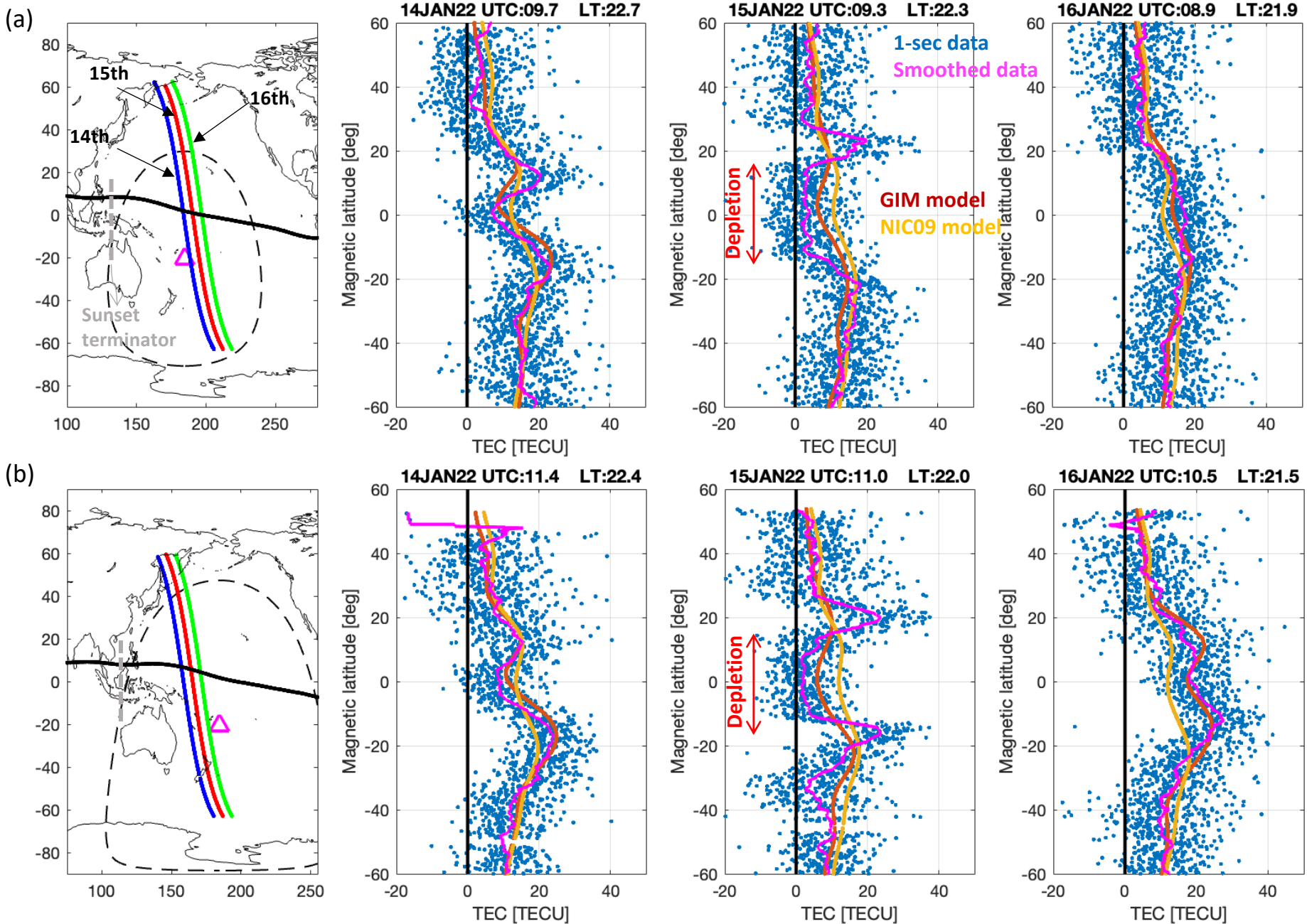
(a)
15th
16th
14th
Sunset
terminator
14JAN22 UTC:09.7 LT:22.7
15JAN22 UTC:09.3 LT:22.3
16JAN22 UTC:08.9 LT:21.9
1-sec data
Smoothed data
GIM model
NIC09 model
Depletion
Magnetic latitude [deg]
TEC [TECU]
(b)
14JAN22 UTC:11.4 LT:22.4
15JAN22 UTC:11.0 LT:22.0
16JAN22 UTC:10.5 LT:21.5
Depletion
Magnetic latitude [deg]
TEC [TECU]

**Figure 4.**

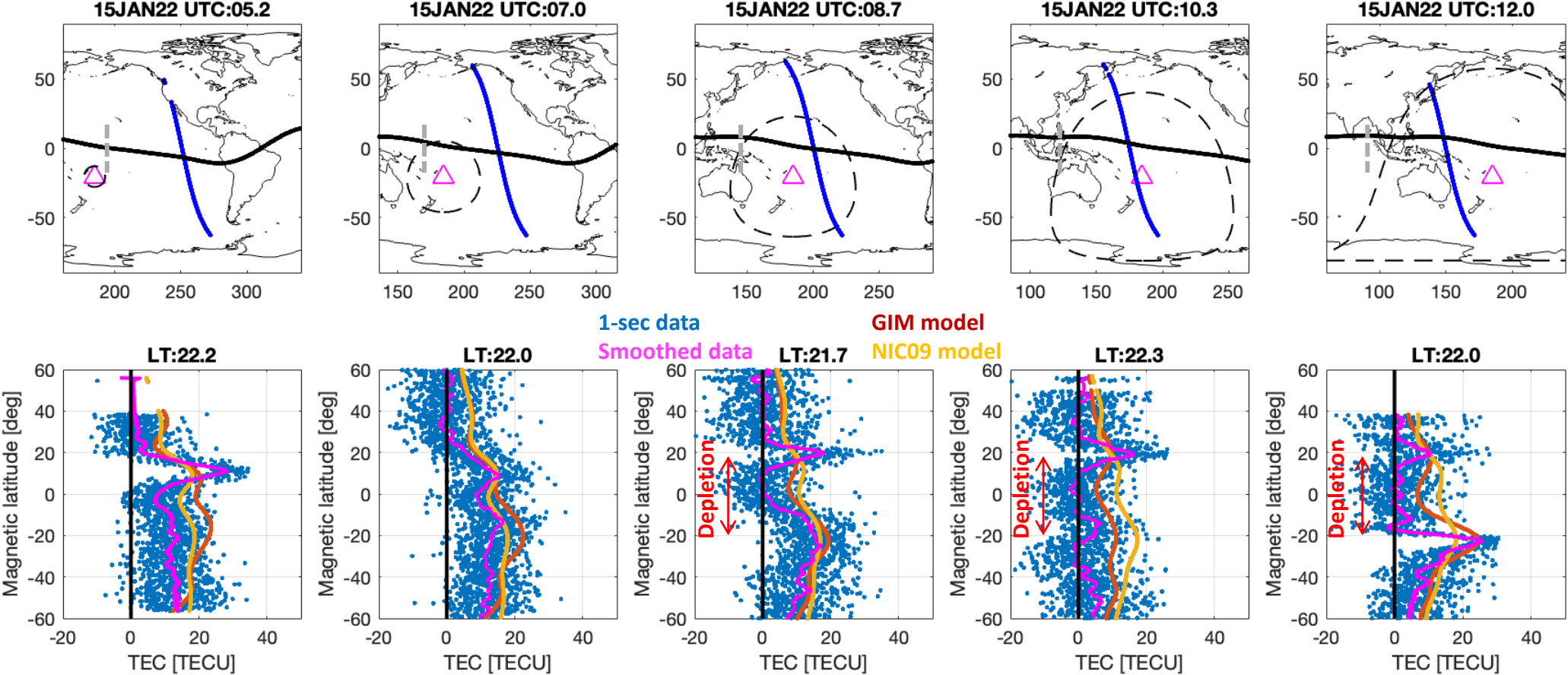
15JAN22 UTC:05.2
15JAN22 UTC:07.0
15JAN22 UTC:08.7
15JAN22 UTC:10.3
15JAN22 UTC:12.0
1-sec data
Smoothed data
GIM model
NIC09 model
LT:22.2
LT:22.0
LT:21.7
LT:22.3
LT:22.0
Depletion
Magnetic latitude [deg]
TEC [TECU]

**Figure 5.**

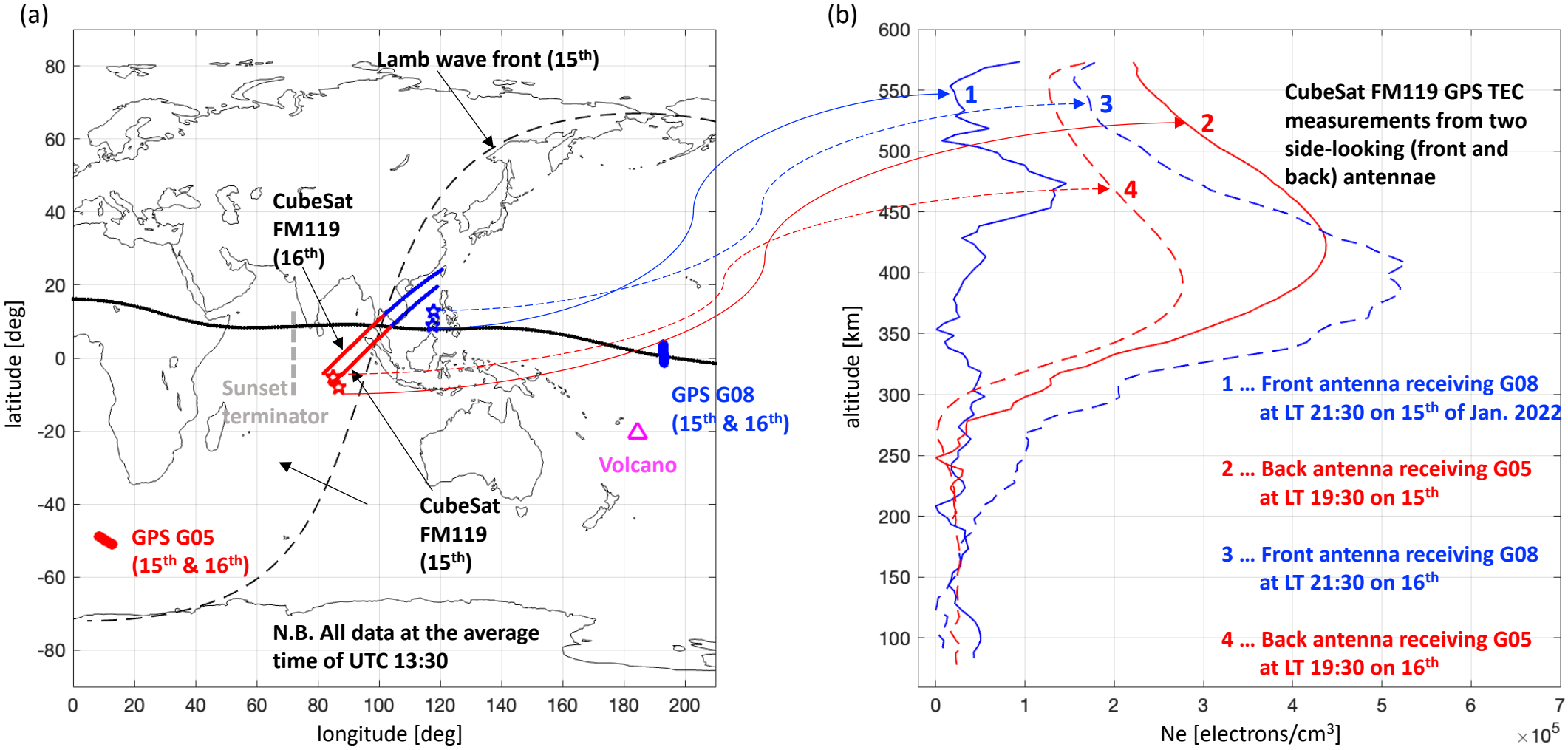
(a)
Lamb wave front (15th)
CubeSat
FM119
(16th)
Sunset
terminator
GPS G08
(15th & 16th)
Volcano
CubeSat
FM119
(15th)
GPS G05
(15th & 16th)
N.B. All data at the average
time of UTC 13:30
latitude [deg]
longitude [deg]
(b)
CubeSat FM119 GPS TEC
measurements from two
side-looking (front and
back) antennae
1 … Front antenna receiving G08
at LT 21:30 on 15th of Jan. 2022
2 … Back antenna receiving G05
at LT 19:30 on 15th
3 … Front antenna receiving G08
at LT 21:30 on 16th
4 … Back antenna receiving G05
at LT 19:30 on 16th
altitude [km]
Ne [electrons/cm3]
×10^5

**Figure 6.**

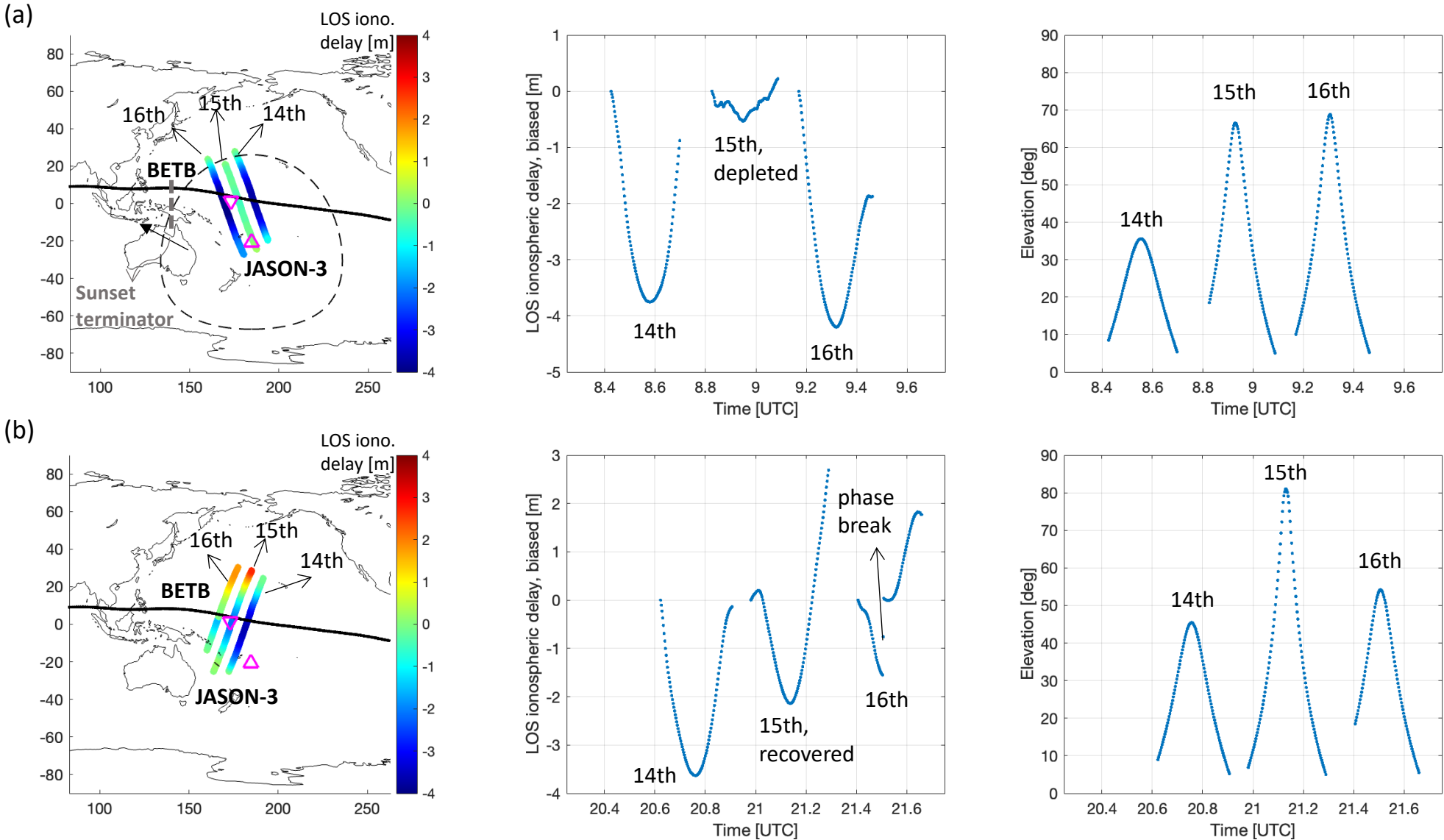
(a)
LOS iono. delay [m]
16th
15th
14th
BETB
JASON-3
Sunset terminator
LOS ionospheric delay, biased [m]
15th, depleted
14th
16th
Time [UTC]
Elevation [deg]
14th
15th
16th
Time [UTC]
(b)
LOS iono. delay [m]
16th
15th
14th
BETB
JASON-3
LOS ionospheric delay, biased [m]
phase break
15th, recovered
14th
16th
Time [UTC]
Elevation [deg]
14th
15th
16th
Time [UTC]

**Figure 7.**

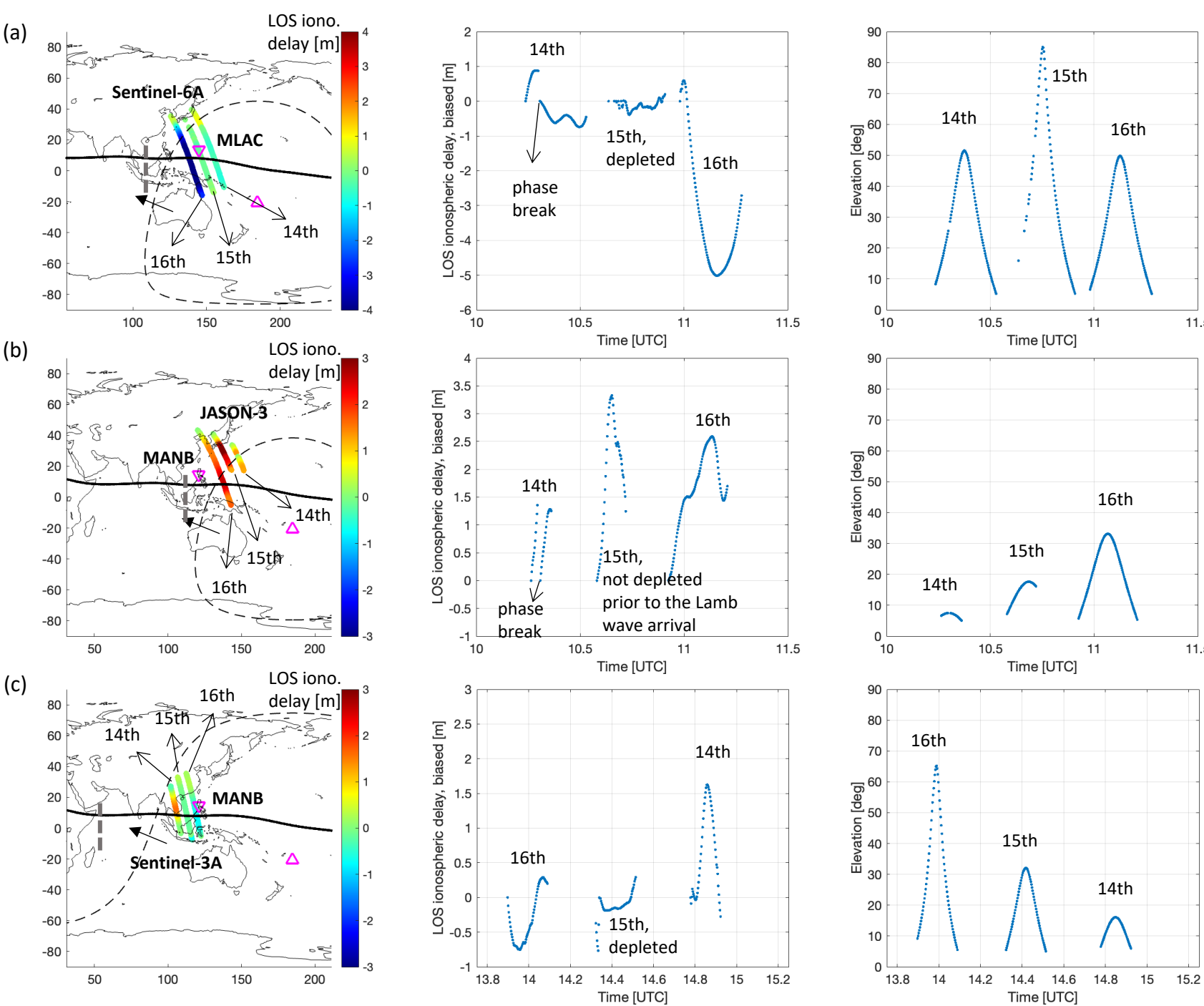
(a)
LOS iono. delay [m]
Sentinel-6A
MLAC
14th
15th
16th
LOS ionospheric delay, biased [m]
14th
phase break
15th, depleted
16th
Time [UTC]
Elevation [deg]
14th
15th
16th
Time [UTC]
(b)
LOS iono. delay [m]
JASON-3
MANB
14th
15th
16th
LOS ionospheric delay, biased [m]
14th
phase break
15th, not depleted prior to the Lamb wave arrival
16th
Time [UTC]
Elevation [deg]
14th
15th
16th
Time [UTC]
(c)
LOS iono. delay [m]
16th
15th
14th
MANB
Sentinel-3A
LOS ionospheric delay, biased [m]
16th
15th, depleted
14th
Time [UTC]
Elevation [deg]
16th
15th
14th
Time [UTC]

**Figure 8.**

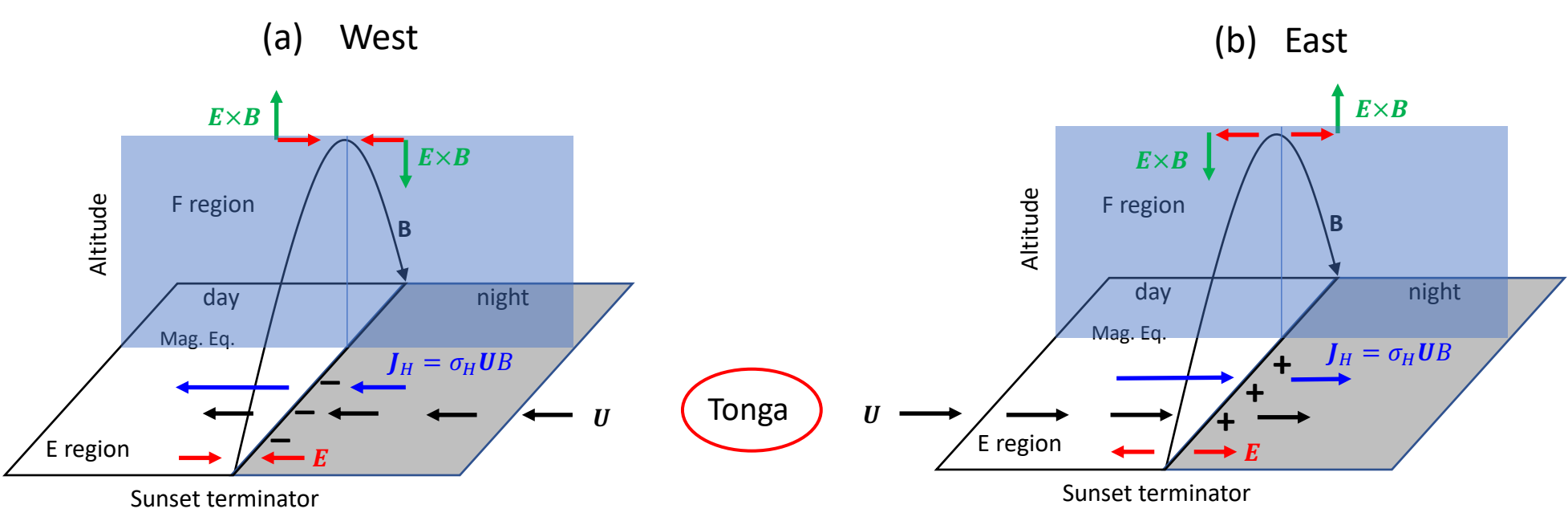
(a) West
E×B
E×B
F region
B
Altitude
day
night
Mag. Eq.
$J_H = \sigma_H UB$
U
E region
E
Sunset terminator
Tonga
U
(b) East
E×B
E×B
F region
B
Altitude
day
night
Mag. Eq.
$J_H = \sigma_H UB$
E region
E
Sunset terminator